Bulletin of the Seismology Society of America, Vol. 99, No. 5, pp. 2681–2703, October 2009, doi: 10.1785/0120080024

Ⓔ

A 3000-Year Record of Ground-Rupturing Earthquakes along the Central North Anatolian Fault near Lake Ladik, Turkey

by J. Fraser, J. S. Pigati, A. Hubert-Ferrari, K. Vanneste, U. Avsar, and S. Altinok

Abstract The North Anatolian fault (NAF) is a ~1500 km long, arcuate, dextral strike-slip fault zone in northern Turkey that extends from the Karliova triple junction to the Aegean Sea. East of Bolu, the fault zone exhibits evidence of a sequence of large ($M_w > 7$) earthquakes that occurred during the twentieth century that displayed a migrating earthquake sequence from east to west. Prolonged human occupation in this region provides an extensive, but not exhaustive, historical record of large earthquakes prior to the twentieth century that covers much of the last 2000 yr. In this study, we extend our knowledge of rupture events in the region by evaluating the stratigraphy and chronology of sediments exposed in a paleoseismic trench across a splay of the NAF at Destek, ~6.5 km east of Lake Ladik (40.868° N, 36.121° E). The trenched fault strand forms an uphill-facing scarp and associated sediment trap below a small catchment area. The trench exposed a narrow fault zone that has juxtaposed a sequence of weakly defined paleosols interbedded with colluvium against highly fractured bedrock. We mapped magnetic susceptibility variations on the trench walls and found evidence for multiple visually unrecognized colluvial wedges. This technique was also used to constrain a predominantly dip-slip style of displacement on this fault splay. Sediments exposed in the trench were dated using both charcoal and terrestrial gastropod shells to constrain the timing of the earthquake events. While the gastropod shells consistently yielded ^{14}C ages that were too old (by ~900 yr), we obtained highly reliable ^{14}C ages from the charcoal by dating multiple components of the sample material. Our radiocarbon chronology constrains the timing of seven large earthquakes over the past 3000 yr prior to the 1943 Tosya earthquake, including event ages of (2σ error): A.D. 1437–1788, A.D. 1034–1321, A.D. 549–719, A.D. 17–585 (1–3 events), 35 B.C.–A.D. 28, 700–392 B.C., 912–596 B.C. Our results indicate an average interevent time of 385 ± 166° yr (1σ).

Online Material: OxCal file to define earthquake timing using radiocarbon dating data.

Introduction

The North Anatolian fault (NAF) comprises the major plate boundary between the Anatolian and Eurasian plates (Fig. 1). The NAF is a right-lateral strike-slip fault zone that extends ~1500 km in an arc across northern Turkey and connects the Karliova triple junction in eastern Turkey to a back-arc extension in the Aegean Sea. The twentieth century sequence of earthquakes along the NAF comprised a series of large ($M_w > 7$) earthquakes that began in A.D. 1939 at the eastern end of the NAF and culminated in A.D. 1999 with a major event that occurred toward the western end of the NAF near Izmit (Hubert-Ferrari *et al.*, 2002). This sequence of earthquakes displayed a well-documented migrating earthquake sequence whereby the strain from one rupture brings the adjacent fault strand to a near critical stress, leading to propagation of strain along the fault (Stein *et al.*, 1997). The relatively simple temporal pattern of faulting along the NAF in the twentieth century may reflect simple elastic strain accumulation in response to tectonic loading in this regime (Hartleb *et al.*, 2003). Whether or not this pattern is a persistent characteristic of the NAF is unknown.

Turkey has a long historical record of seismic activity along the NAF, documented by major damage to population centers that are situated near the fault zone, including significant loss of life and extensive damage to infrastructure

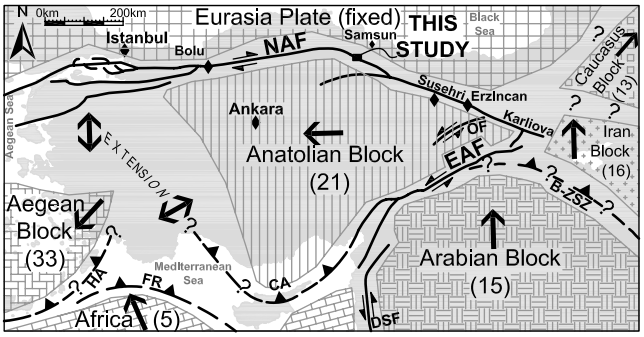

Figure 1. Schematic tectonic model of the Eastern Mediterranean region (Şengör *et al.*, 2005; Hartleb *et al.* 2006; Reilinger *et al.*, 2006). Arrows depict the approximate direction of plate movement with the rate of movement in parentheses (mm/yr). All plates shown have a clockwise rotation relative to the Eurasian Plate. Key: North Anatolian fault (NAF), East Anatolian fault (EAF), Dead Sea fault (DSF), Bitlis-Zagros suture zone (B-ZSZ), Cyprean Arc (CA), Florence Rise (FR), and Hellenic arc (HA).

(Ambraseys, 1970; Ambraseys and Finkel, 1987, 1995, Ambraseys and Jackson, 1998; Ambraseys, 2001; Guidoboni *et al.*, 1994; Guidoboni and Comastri, 2005). The historical record, which covers much of the past 2000 yr, appears to show some cyclicity (Fig. 2, Table 1) but is incomplete, and in many cases historical reports of ground shaking cannot be attributed to specific fault strands or segments. Investigations using geomorphology and paleoseismic trench studies can provide additional data about past earthquakes along the NAF. Trench studies utilize detailed interpretation of the stratigraphy of sediments deposited on or near faults to determine the timing and size of ground-rupturing earthquakes. Therefore, determining the rupture history through paleoseismic investigations in conjunction with the historical record of earthquakes provides the best method for expanding our knowledge of NAF earthquakes.

This investigation was undertaken on a strand of the NAF striking along the northern side of the valley that runs between Lake Ladik to the west and the village of Destek to the east (hereafter referred to as the study area, Fig. 3). Lake Ladik occupies a depression that appears to have formed at an extensional stepover, or fault bend, that is ~2 km wide and is situated at the eastern end of the Havza-Ladik Basin (Barka and Hancock, 1984). Destek is situated at the western edge of the Tasova-Errba pull-apart basin (Barka *et al.*, 2000), a structure associated with an extensional step in the NAF, which also formed the adjacent Niksar Basin.

The Seismotectonic Setting section of this article describes the seismotectonic setting of the central NAF where this study was conducted, and the Destek Site Description section describes the geomorphic features nearer to the trench site. The Methods section provides a brief outline of the methods we employed to establish the distribution, genesis, and age of the strata revealed by excavating a paleoseismic trench. The Results section first describes the stratigraphy we encountered in the trench by conventional visual paleoseismic trench logging before introducing the results of a magnetic susceptibility survey and finally describing the evidence for, and age of, earthquakes identified by this study. The Discussion and Conclusions sections, respectively, discuss and conclude the results from this study.

Seismotectonic Setting

The Anatolian plate is being extruded westward due to the collision of the Arabian and Eurasian plates. At the Karliova triple junction, the NAF converges with the East Anatolian fault (EAF), which is a conjugate left-lateral strike-slip fault at the eastern border of the Anatolian plate. Most of the deformation associated with the extrusion is accommodated along discrete fault zones that comprise the NAF and the EAF. Extensional structures in the western Anatolian plate and in the Aegean extensional domain may be formed in response to slab rollback at the Hellenic arc subduction zone that has produced a back-arc extensional regime (Faccenna *et al.*, 2006). Very little deformation is occurring within the eastern portion of the Anatolian plate (Anatolian Ova domain; Bozkurt, 2001).

Recent (twentieth century) fault ruptures along the NAF have had relatively long rupture lengths east of Bolu and have occurred in quick succession, which probably reflects a simple fault geometry (Barka and Kadinsky–Cade, 1988). In contrast, recent fault rupture lengths are shorter west of Bolu, and the duration between events on subsequent segments has been longer in this area (Fig. 2). This complex segmentation in the western Anatolian microplate probably reflects a higher degree of fault complexity (relative to the eastern NAF) that is related to the stress associated with back-arc extension of the Hellenic arc (Flerit *et al.*, 2004).

The total amount of displacement across the NAF plate boundary has been estimated on a variety of spatial and temporal scales. On a continental scale, it appears that the NAF nucleated in the east and propagated westward. Şengör *et al.* (2005) determined that the NAF formed ~11 m.y.a. in the east, and Şengör and Canitez (1982) estimated the total offset to be 50–100 km near the eastern end of the fault. These studies suggest that the NAF formed no earlier than 200 k.y.a. in the west, and that total offset near the Sea of Marmara is only ~30 km. The total amount of offset along the fault strand in our study area has not been determined, but nearby studies of offset along the NAF on a regional scale suggest total displacements of ~30–75 km. For example, east of the study area, between the town of Turhal and the Amasya Plain, the geometry of the Yesilirmak River suggests a total offset of ~30 km (Şengör *et al.*, 2005). West of our study area, between the Amasya plain and Lake Ladik, offset of the same river suggests at least 50 km of offset (Şengör *et al.*, 2005). A proposed stream-capture scenario for this same area indicates a total offset of as much as 75 km (Hubert-Ferrari *et al.*, 2002).

Constraints on the rates of displacement across the NAF come from Global Positioning Systems (GPS), as well as geomorphic and geologic evidence. Over long time periods

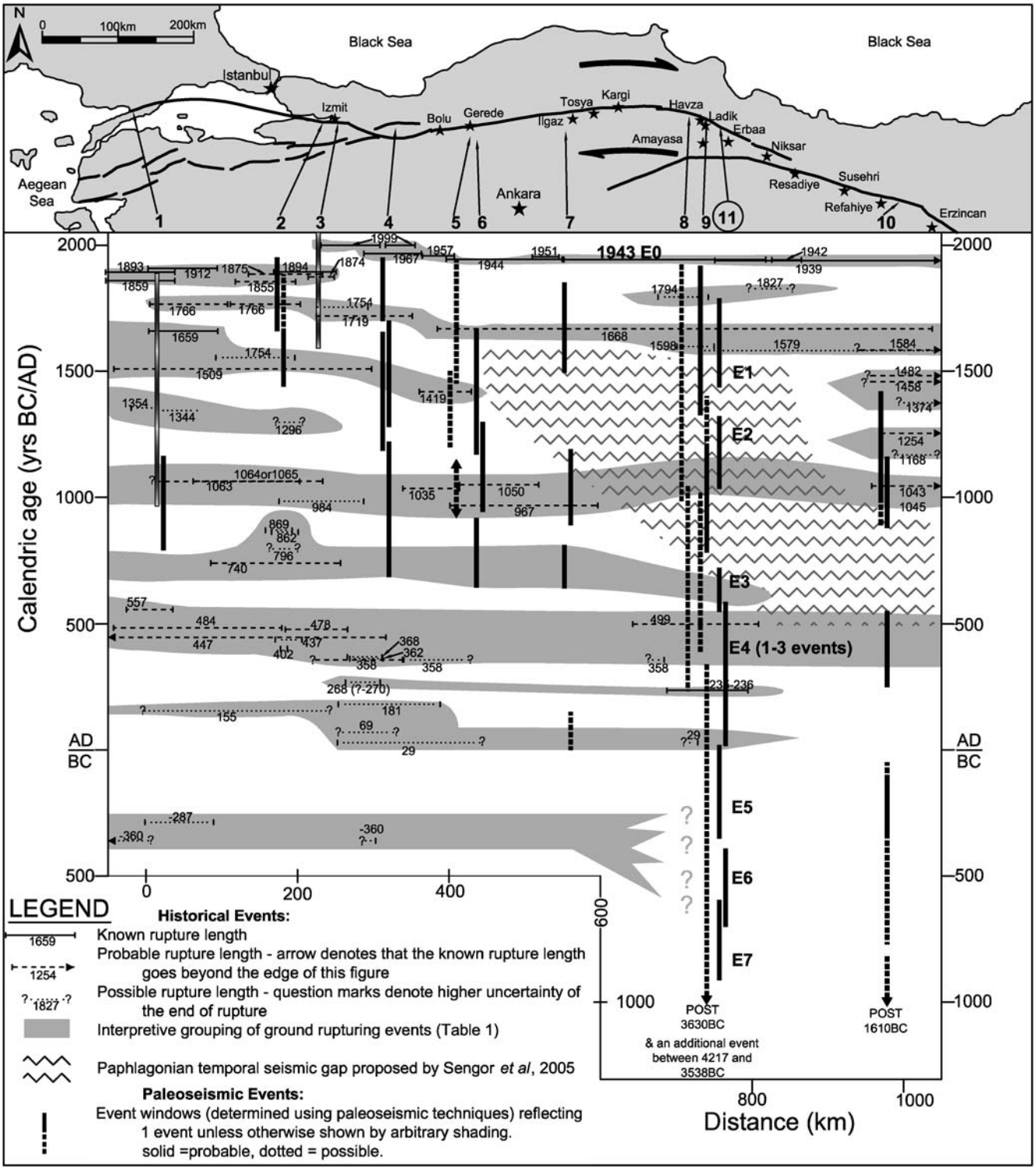

Figure 2. Summary of historical records and paleoseismic investigations (including this study) of ground-rupturing earthquakes along the NAF. Lower panel: Historical events are depicted with horizontal lines that represent the approximate rupture length (after Şengör *et al.*, 2005). Results of individual paleoseismic investigations are depicted by vertical lines that reflect the event windows. In the cases where multiple events are interpreted in a single temporal window, the approximate number of events are shown by shading. Upper panel: Site locations of key paleoseismic investigations: (1) Kavakkoy (Rockwell, Barka, *et al.*, 2001), (2) Golcuk (Klinger *et al.*, 2003), (3) Kosekoy (Rockwell, Aksoy, *et al.*, 2001), (4) Duzce (Pucci, 2006), (5) Demir Tepe (Kondo *et al.*, 2003), (6) Gerede (Okumura *et al.*, 2003), (7) Ilgaz (Sugai *et al.*, 1999), (8) Havza (Yoshioka *et al.*, 2000 in Hartleb *et al.*, 2003), (9) Alayurt (Hartleb *et al.*, 2003), (10) Cukurcimen (Hartleb *et al.*, 2006), and (11) Destek (this study). Where the NAF splays near Niksar and west of Bolu, the historical data portray all fault strands as one, whereas the paleoseismic data are strand specific as indicated by arrows to locations on the map.

Table 1
Summary of Earthquake Clusters Identified along the NAF*

Cluster	Complete Cycle?	Beginning		End	
		Time (Century)	Location	Time (Century)	Location
1	Yes	A.D. 1939	East	Ongoing	West
2	Yes	Late eighteenth	East	Early twentieth	West
3	Yes	Late sixteenth	East	Middle eighteenth	West
4	No	Late fourteenth	East	Middle seventeenth	West
5	No	Middle twelfth	East	Middle fourteenth	West
6†	No	Middle tenth	—	Middle eleventh	—
7	No	Middle sixth	Center	Middle ninth	West
8†	No	Middle fourth	—	Middle sixth	—
9	No	Middle third	East	Middle third	West
10	No	Early first	East	Middle second	West

*Limited to the last 2000 yr. Refer to Figure 2 for details.
†Nondirectional

dextral strike-slip rates of approximately 18 ± 5 mm/yr (10–12 ka; Hubert-Ferrari *et al.*, 2002) and $18.6 + 3.5/-3.3$ mm/yr (~3 ka; Kozaci *et al.*, 2009) have been estimated using offset geomorphic features. Geomorphic studies over shorter time periods undertaken on the Tosya earthquake rupture segment determine higher rates in the order of 20.5 ± 5 mm/yr over the last 2–2.5 ka (Kozaci *et al.*, 2007), suggesting a higher rate of displacement in the recent past. A block model constrained by GPS data indicate dextral strike-slip rates of 24.0–28.3 mm/yr and dip-slip rates of 8.2 mm/yr compressive to 13.2 mm/yr extensional along the NAF (Reilinger *et al.*, 2006). Near our study area, the same block model estimates a regional dextral strike-slip rate of 25.8 ± 0.2 mm/yr and a dip-slip rate 0.2 ± 0.2 mm/yr extensional (Reilinger *et al.*, 2006). These modeling results indicate that, at a regional scale (10 to 100s of kilometers), this section of the NAF can be characterized as a simple strike-slip structure.

The study area is located near the eastern end of an approximately 280 km long segment of the NAF that ruptured in the 1943 M 7.4 Tosya earthquake (Fig. 2) also known as the Ladik earthquake (Ambraseys, 1970; Barka, 1996; Ambraseys and Jackson, 1998). The penultimate event on this fault segment may have been an event in A.D. 1794 (Ambraseys and Finkel, 1995) or the large A.D. 1668 event that ruptured from approximately Erzincan to Bolu (Şengör *et al.*, 2005). Lettis *et al.* (2002) concluded that stepovers of 4 to 5 km arrest fault rupture regardless of displacement, and the Niksar pull-apart basin has a width of approximately 10 km. Therefore, based on reports of earthquakes over that period from Ankara (Ambraseys and Finkel, 1995), and the stepover width of the Niksar pull-apart basin, it is likely that the A.D. 1668 event actually consisted of a series of events that were spaced closely in time during July and August.

A large earthquake occurred in A.D. 1598 in the vicinity of Amasya and caused massive damage along the Black Sea coastline (Ambraseys and Finkel, 1995). Several ancient documents refer to an earthquake event or series of events that occurred between A.D. 523 and 543 in Amasya and other Turkish cities (Guidoboni *et al.*, 1994). Ambraseys and Jackson (1998) document an event that occurred near Niksar in A.D. 499, although they clearly state that there is a large degree of uncertainty concerning the location of this event. Other ancient documents suggest a large earthquake occurred at Neocaesarea (Niksar) in A.D. 343, although one of the documents mentions that Niksar was engulfed by the sea during this event, which is very unlikely given the 60 km distance to the Black Sea (Guidoboni *et al.*, 1994). However, it is possible that this refers to flooding caused by displacement of the Kelkit River, or possibly a dam failure. Finally, an epitaph dating to A.D. 235–236 records the death of a child due to an earthquake in Amasya, which suggests, along with other documentation, that another earthquake event that was strong enough to destroy buildings occurred near Amasya at this time (Guidoboni *et al.*, 1994; Ambraseys and Jackson, 1998).

Together, these historical data indicate that there is an apparent paucity in seismic activity between the sixth and sixteenth centuries A.D. between Bolu and Refhiye, which includes our study area (Fig. 2). Şengör *et al.* (2005) named this spatiotemporal window the Paphlagonian temporal seismic gap (PTSG) with the caveat that it could represent either a paucity in seismicity or an absence of earthquake information in the historical record prior to the seventeenth century. However, the fact that a large event or series of events ruptured the NAF between Erzincan and Bolu in A.D. 1668 does suggest that there may have been a long duration of seismic quiescence and strain accumulation preceding this event.

Regardless, it is well known that the historical record is incomplete, and many of these events are based on sparse or even singular data sources. The strongest level of certainty comes from overlapping data from multiple historical accounts and clear temporal windows established in paleoseismic investigations. To date, the closest paleoseismic investigations to the Destek site are located at Alayurt (Hartleb *et al.*, 2003) ~25 km to the northwest, Havza (Yoshioka *et al.*, 2000) ~45 km to the northwest, Ilgaz (Sugai *et al.*, 1999) ~210 km to the west, and Cukurcimen (Hartleb *et al.*,

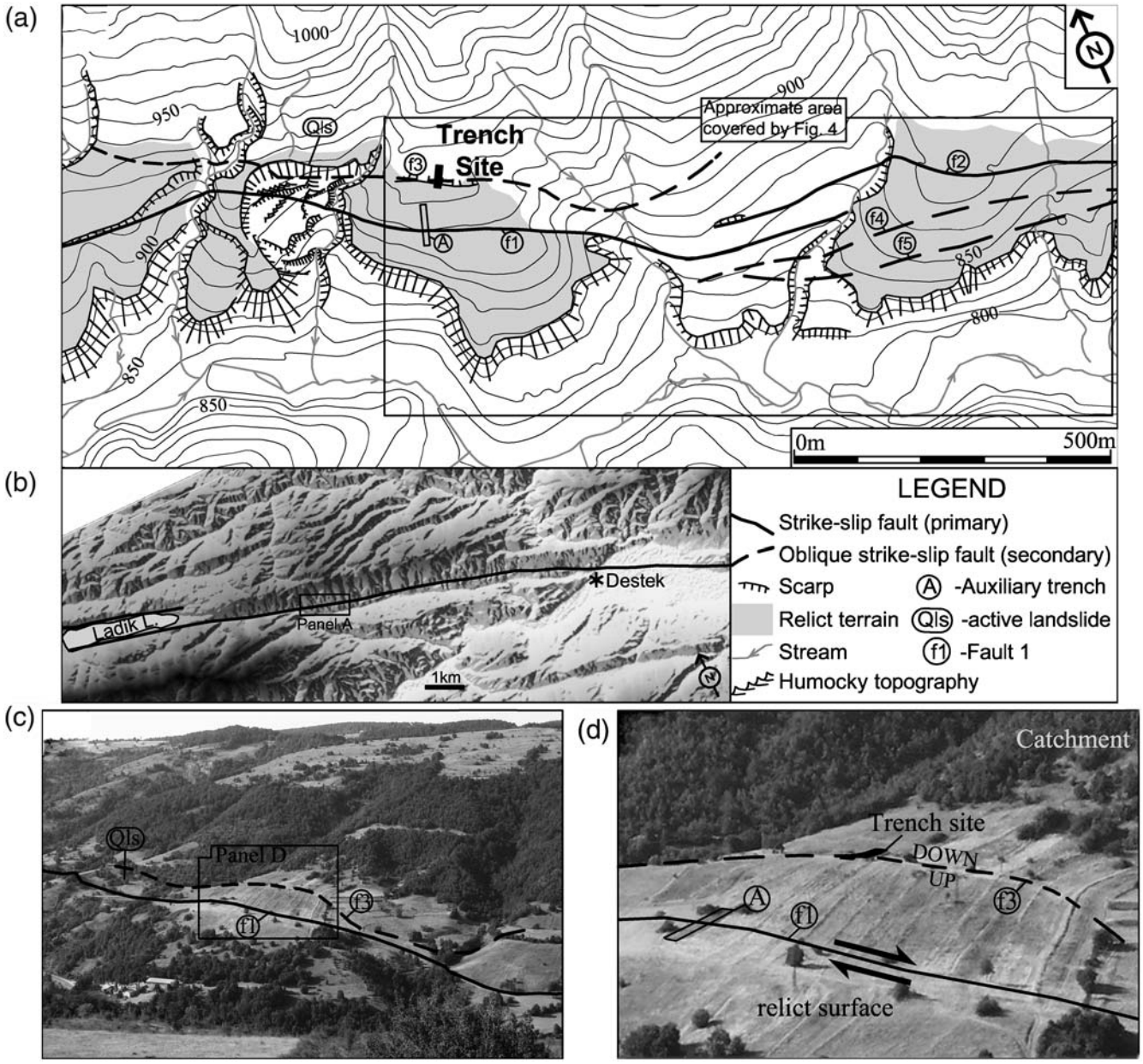

Figure 3. Geomorphic map of the Destek paleoseismic trench area. Contour interval is 10 m. The length of perpendicular ticks on the scarp line type depicts the map area covered by the scarp. Panel C is an annotated oblique photograph taken from the opposite side of the valley taken toward approximately north-northwest. Panel D is a larger scale view of the trench area from the same photo as panel C. The landslide (labeled Qls) is active, the scarp is drawn on panel A, and head scarp is in alignment with fault f3. The trench site is situated at 40.868° N, 36.121° E.

2006) ~260 km to the east (Fig. 2). The relationships between temporally constrained events at these four locations and those at our study site are discussed in the Event Timing Relative to Other Studies section.

Destek Site Description

The Destek paleoseismic trench was excavated ~2.7 km northwest of the town of Destek across a strand of the NAF (Fig. 3b). The geomorphology near the Destek trench is dominated by an axial drainage that runs subparallel to the strike of the fault zone and cross-axial drainages that generally run subperpendicular to the strike of the fault zone. The axial drainage is positioned south of the fault zone and drains toward the east at a slope of ~2°. The trench site is situated on the north side of the valley, so the nearby cross-axial drainages drain to the south (Fig. 3a).

The geomorphology near the study area is dominated by three distinct landscape types: hill terrain, relict terrain, and reactivated terrain, which have moderate, low, and high rates of erosion, respectively (Fig. 3a,c,d). Hill terrain typically has relatively steep slopes covered by regenerating forest vegetation, but some flatter areas are utilized for agriculture. Slope gradient generally controls the distribution of soil with

steeper slopes having thin to no soil, and gentle slopes have accumulated soils up to ~1 m thick. Several recent shallow (> 5 m) regolith slide-and-flow failures were recognized outside the area covered by Figure 3. Relict terrain consists of side-hill benches and gentle concaved slopes that extend from the hill terrain into the valley where it is incised by the reactivated terrain. Soils of the relict terrain are typically residual soils with thin topsoil, but at some locations slopewash from the hill terrain is deposited on the surface. These surfaces are used extensively for agriculture and grazing. Extensive deep (> 5 m) failures of this surface are common, especially adjacent to the cross-axial drainages, and head scarps are common along the fault zone. These scarps probably reflect the presence of fault-weakened materials and are considered to be part of the reactivated terrain. The side-hill benches are in part due to tectonics, but an overall ~2° slope toward the east of isolated relict surfaces recognized between the eastern end of Lake Ladik (1030 m) and Destek (750 m) strongly suggests that this surface is associated with a drainage system that previously flowed from the Havza-Ladik basin eastward into the Tasova–Erbaa basin. Reactivated terrain areas buffer axial and cross-axial drainages and are incised into hill and relict terrains. This terrain is predominantly heavily vegetated and not used for agriculture because of extensive erosion. The high rates of geomorphic activity and often steep erosive slopes in the reactivated terrain generally inhibit the formation of soil in this area. Reactivated terrain is typified by extensive, recent, and active slope failures, especially adjacent to the cross-axial drainages. Deep rotational block failures of the relict terrain are also common adjacent to the cross-axial drainages (e.g., active landslide [Qls] in Fig. 3a,c) and evidence for small, shallow slide-and-flow failures was observed near the study area. The cause of these failures appears to be removal of lateral support by knick-point migration up the cross-axial streams related to incision of the Destek River. Local faulting has weakened materials, caused stream capture and trapped ground water, all of which further exacerbate slope instability near the fault zone.

Fault scarps are clearly recognizable on the relict surface but not in the hill and reactivated terrain because of the high rates of geomorphic activity in the reactivated terrain and the absence of faulting in the hill terrain. The cross-axial drainages are clearly affected by faulting; however, no clear patterns were observed, and there is a lack of datable materials to determine rates of offset. Geomorphic mapping indicates that the fault zone strikes at ~118° west of the trench site and at ~109° east of the site, causing a ~9° transpressive (concaved to the south) bend in the fault. This bend, along with a dilational step in the fault, has caused a paired pop-up structure (Fig. 4).

An auxiliary trench (Fig. 3a,d) was opened across the southern extent of the pop-up structure that exposed a broad (> 30 m) deformation zone of highly sheared and extremely weathered rock that is overlain by a thin topsoil. Despite the absence of a well-defined fault scarp, this strand labeled f1 in Figures 3 and 4, is interpreted to be the main strike-slip fault. We did not conduct detailed logging of sediments exposed in this trench because the lack of recent deposits overlying the fault zone limited its potential for yielding paleoseismologic information.

The primary trench excavated as part of this study is located on the northern side of the pop-up structure where a fault (labeled f3 in Figs. 3 and 4) has formed a well-defined uphill-facing scarp and a sediment trap. The trench revealed an apparent normal displacement. Because the northern fault strand (f3) is situated ~100 m to the north of the main fault (f1), we think that the dip of the f3 fault plane bends southward with depth to connect to the main f1 fault plane. Therefore, we interpret fault f3 to be an overturned thrust splay of the primary strike-slip fault. This strand appears to be the northern limit of a pop-up structure formed by a localized transpressive regime. The overturned nature of the fault may reflect southward deflection of the fault near the surface, possibly because of the load caused by the hills immediately to the north of the fault (Berrill, 1988) or adoption of a preexisting structure. Nonetheless, it is also possible that fault f3 is a normal fault that accommodates horizontal or subhorizontal compression in the northern wall of the fault zone. Because we study one of

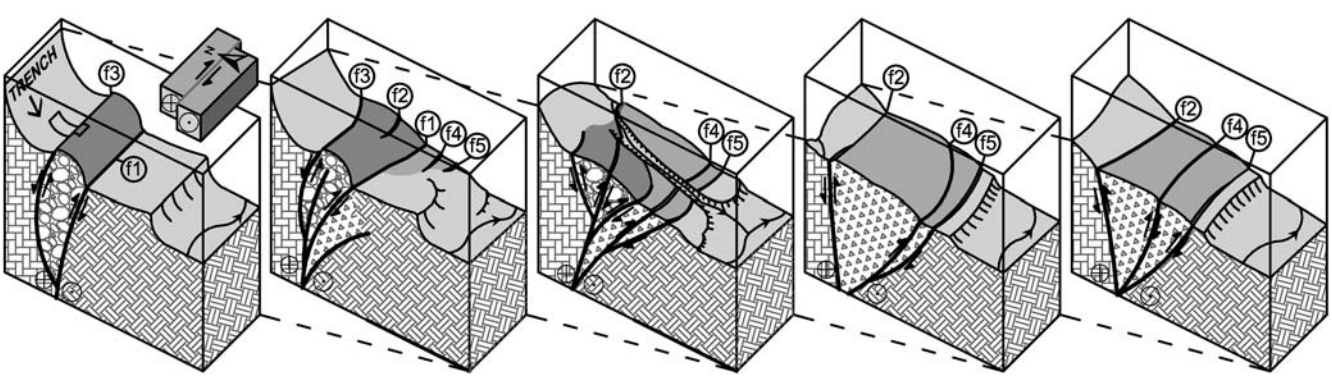

Figure 4. Schematic sliced and offset box diagram of the interpreted local tectonic setting at the Destek paleoseismic trench site. The approximate location of this model is shown on Figure 3.

multiple fault strands, we may not have a complete earthquake record for this segment of the fault.

Upslope of the sediment trap is a small (~0.02 km^2) unchannelized catchment area in the hill terrain. The upper half of this catchment area is dominated by tree and shrub vegetation with outcrops of extremely weathered rock present at the surface. Overland flow associated with moderate to large rainfall events probably accounts for the bulk of sediment erosion and transport (no channel forms were recognized), but small (1–10 m^3) debris flows may also occur. The role of tree throw is not well understood in the absence of local records of vegetation cover. The lower half of the catchment area is covered by grassland and acts as a trap for sediment being eroded from the upper half of the catchment area.

Methods

Conventional Paleoseismic Investigation

Conventional paleoseismic trench logging utilizes qualitative descriptions of stratigraphic units and quantitative graphing of their distribution in excavated or existing exposures across or adjacent to faults. Many paleoseismic investigations have been conducted previously on the NAF (Okumura *et al.*, 1993, 1994; Sugai *et al.*, 1999; Yoshioka *et al.*, 2000; Rockwell, Aksoy, *et al.*, 2001; Rockwell, Barka, *et al.*, 2001; Hartleb *et al.*, 2003; Kondo *et al.*, 2003; Okumura *et al.*, 2003; Kondo *et al.*, 2005; Hartleb *et al.*, 2006; Pucci, 2006; Kozaci *et al.*, 2007; Palyvos *et al.*, 2007) and globally on all styles of faults (i.e., McCalpin, 1996), which provide precedents that were followed in this study.

Our trench is 5.5 m wide at the southern end wall, with approximately parallel side walls that are 17 m long, and has a maximum depth of about 5 m. Each wall is composed of two subvertical walls that are 1.5–2.5 m high and separated by a subhorizontal bench ~1 m wide. We use the terms upper and lower to describe the section of the wall above and below the bench, respectively. A string grid (1 × 1 m) was erected on the trench walls and held in place with nails at each node; accuracy was maintained using a laser level base station. Conventional descriptive logging was performed on sediments exposed in the upper and lower, east and west walls (Fig. 5). We also took photographs of each grid cell that were later corrected for spherical divergence and perspective. Figure 6 shows a close-up photo log of the fault zone overlain with the boundaries from field logging (Fig. 5). There are subtle differences between the boundaries evident on the photo log (Fig. 6) and the lines from the field logging; this is a consequence of the roughness of the trench face and the effect of parallax on the photos. The unit boundaries north of the fault are very subtle and are not obvious in the photo log; therefore, we have not presented the photo log of the entire trench.

Magnetic Susceptibility Investigation

Paleoseismic investigations generally rely on graphical logs and qualitative descriptions of sediments exposed in paleoseismic trenches. As part of this study we measured magnetic susceptibility (MS) on the trench walls to determine if it could provide useful additional quantitative information on the nature and distribution of the exposed sediments. MS is a measure of how a material's magnetic permeability differs from that of free space; therefore, it is a dimensionless value (we used SI values in this study). Magnetic permeability is a measure of the ability of a material to become magnetized in the presence of a magnetic field. The MS of a soil is mainly controlled by its mineralogy but is also influenced by temperature, grain size and shape, and moisture content. Magnetite has the highest MS values, although maghemite, hematite, ilmenite, pyrrhotite, and pyrite also contribute to the measured MS signal; hereafter, these minerals are collectively referred to as iron minerals. Details of the magnetic susceptibility method are described in Appendix A.

Chronology

We collected 158 samples of charcoal and 138 samples of terrestrial gastropods (predominantly Monarcha species) from the trench. We also collected several fragments of slag, brick, crockery, and bone but did not submit them for chronologic analysis. Our sampling strategy was twofold; first, samples were selected to constrain the chronology of the sedimentary sequence focusing on the age of the event horizons, and second, the utility of ^{14}C dating of minute gastropods was evaluated due to their abundance and potential utility at Destek and other sites nearby. Details of the dating methodology are described in Appendix B.

Results

Trench stratigraphy

South of the Fault. South of the fault zone, the trench exposed mostly highly sheared rock on the upthrown side of the fault. The west trench wall revealed highly sheared, weathered rock that grades up into residual soil that retains some fabric of the parent rock material. A large block (~0.8 m^2) of extremely weathered rock or saprolite is contained within the residual soil near the south end of the wall (Fig. 5). This block is probably a remnant of bedrock that has weathered at a lower rate than the adjacent units and has, therefore, retained some of its original lithification. Residual soils are not exposed on the east wall, but the exposed rock is more weathered toward the surface. A thin layer of topsoil mantles the residual soil on the west wall and the rock on the east wall. We were not surprised by the variation in materials exposed on each wall of the trench because the bedrock is commonly very faulted and composed of a range of different materials in the fault damage zone.

Fault Zones. The fault zones exposed on each wall are quite different. On the west wall, for example, the fault zone is ~1.2 m wide near the surface and ~3 m wide at the base of the trench. It is composed of two distinct sets of faults, the

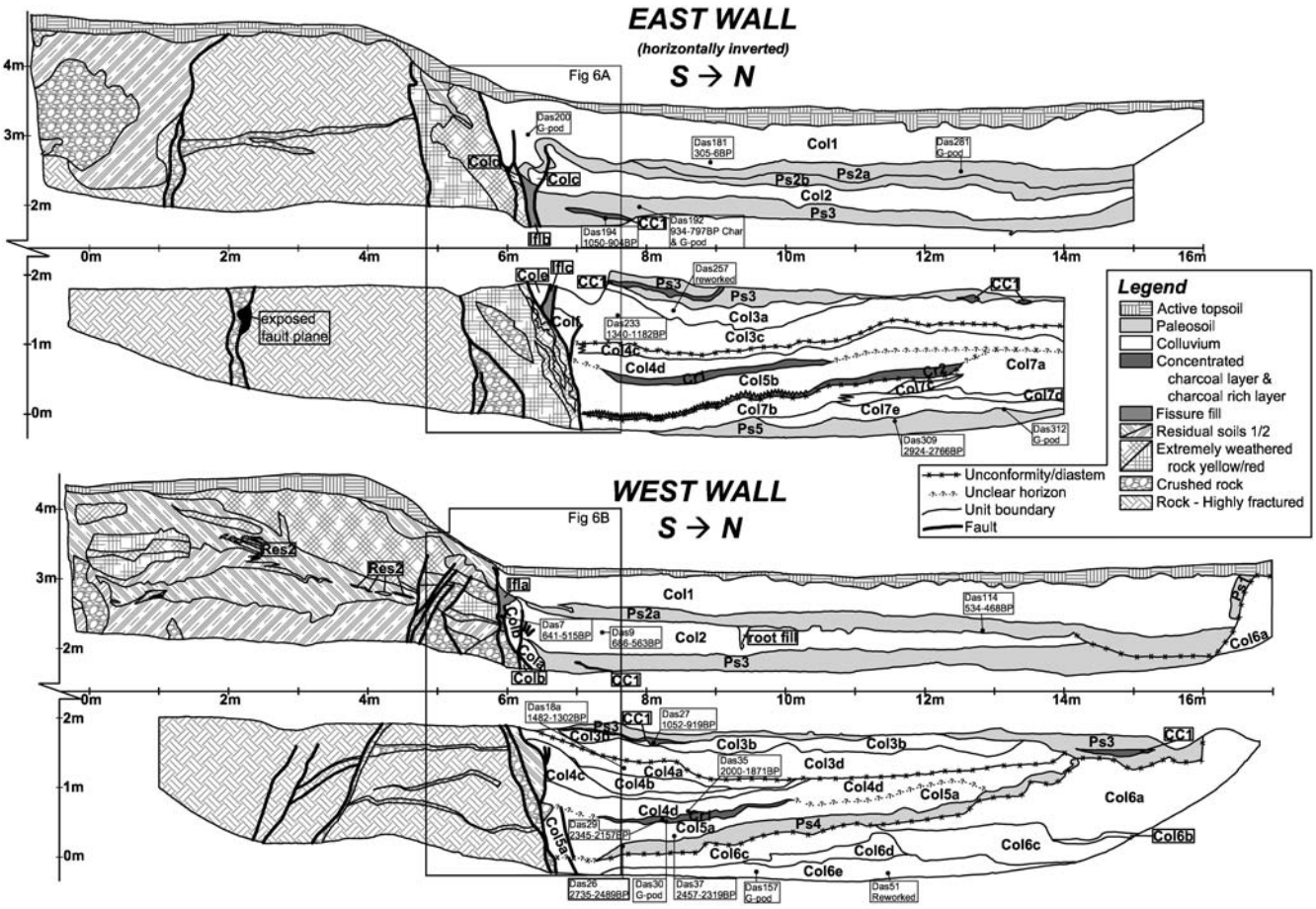

Figure 5. Paleoseismic trench logs for the east and west walls of the Destek trench. Bench levels are represented by a gap on each wall (benches were ~1 m wide). The west wall log is plotted with the same perspective as logged in the field; the east wall log is horizontally inverted for clarity. The legend provides a simplified description of trench units and symbols; detailed descriptions are given in Appendix C. We have not presented the radiocarbon ages of the gastropods (*G*-pod). Ages shown in boxes are the maximum and minimum ages (years B.P.) inside the 2σ standard deviation (or incorporating 95% of the uncertainty) associated with the age after we have modeled the strata in the OxCal program (Fig. 10). Individual sample numbers are shown above the ages.

northern set dipping to the north and the southern set dipping to the south. Crushed rock, residual soil, and extremely weathered bedrock are exposed between the fault strands on the upper wall, and subhorizontal zones of crushed rock are exposed on the lower wall. On the east wall, the fault zone is ~5 m wide with the southern fault set dipping near vertically and incorporating some crushed rock. The northern fault set is composed of faults and associated splays that are separated by extremely weathered and crushed rock and a small amount of residual soil. On both walls, the northern side of the fault zone is characterized by minor fault strands splaying into the adjacent sedimentary sequence. The local geomorphology and the juxtaposition of rock against modern sediments indicate that the northern strands of the fault, exposed on both walls of the trench, are the modern locus of shear. The southern strands of the fault zone exposed in both walls are interpreted to be a synthetic shear that splays off the main fault trace exposed in the trench (f3) and extends into the pop-up structure toward the main strand of the fault zone (f1, Fig. 3).

North of the Fault Zone. There are similar stratigraphic sequences, or packages, of colluvium and paleosols exposed on both trench walls north of the fault zone. In the following discussion, we use the term paleosol (designated as Ps) to refer to units with a relatively high level of organic content that reflects a slower rate of sediment accumulation and/or a longer period of time spent at the ground surface. We use the term colluvium (designated as Col) to describe the allocthonous materials with low organic content that are derived from adjacent slopes. The term package describes a subset of connected units and is referred to by numerals amended to unit labels (e.g., Col5a and Col5b comprise the package Col5). In the following sections we discuss the sequence of both walls simultaneously, starting at the surface, and refer to units with the same symbols used in Figures 5–7. When we refer to specific features exposed in the trench walls, we also give the horizontal (H:#) and vertical (V:#) coordinates, which are expressed in meters from the bottom of the southern end of the trench. In this section we describe the sediments;

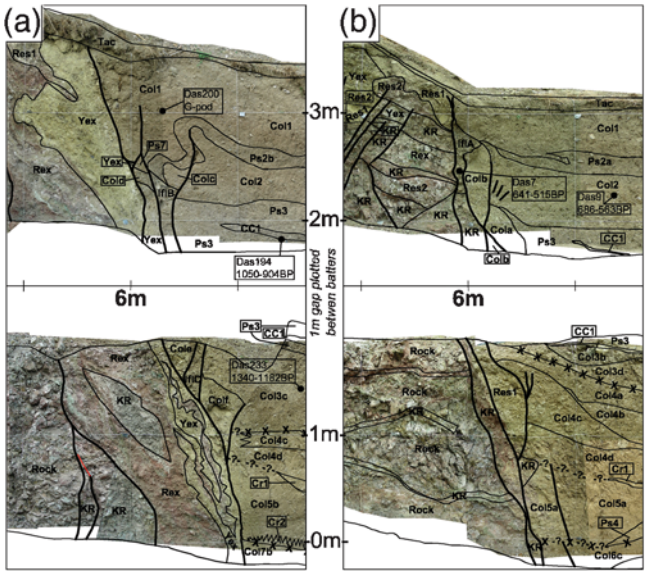

Figure 6. Close-up of the fault zone with a photo log background. Panel A is the east wall (horizontally inverted), and panel B is the west wall, and on both panels, north is to the right. The legend from Figure 5 applies to this figure, and detailed descriptions corresponding to the symbols in each unit are presented in Appendix C. Marginal stability of the trench in the fault zone resulted in minimal cleaning of the trench surface, as a result the photo log does not match the lines perfectly due to the effect of parallax. The photos provide enough detail to show that it is very difficult to see any strata north of the fault zone and highlight the large degree of uncertainty associated with using fault terminations to distinguish event horizons in this trench.

the evidence for paleoseiosmic events is described in the Event Stratigraphy and Chronology section.

Most of the units we discuss have a similar geometry on both walls of the trench. The upper opposing walls are about 5.5 m apart; therefore, most of these deposits have a sheet like geometry. We recognized no channel forms in the catchment area geomorphology and no channelized flow deposits in the trench exposure. We, therefore, suggest that most of the alocthonous materials (e.g., colluvium) were transported and deposited by sheet flow.

The exposed sediment sequence is capped with topsoil (Tac), which is continuous across the fault and shows no signs of rupture. Beneath the topsoil is Col1 although on the upper west wall near H:16.5 is Ps1. Ps1 probably formed at the same time as the Ps2 package, but we cannot rule out a younger or older age. The Ps2 package underlies Col1 and consists of Ps2a and Ps2b on the east wall and Ps2a on the west wall, which are stratigraphically equivalent. Ps7 (Fig. 6a) is probably equivalent to Ps2b. Ps2b and the base of Col1 are deformed on the upper east wall at H:6–7 (Fig. 6a). The tops of several fissure fills are present at about this stratigraphic location; these are discussed further in the Event Stratigraphy and Chronology section.

Col2 thins, and Ps2a thickens, away from the fault in both the west and east walls. A wedge-shaped tree root fill is exposed in the east wall at ~H:9.5 and probably formed during the deposition of the overlying Ps2a as evidenced by the absence of a root cavity above the paleosol. Colc and Cold were probably parts of Col2 prior to tectonic deformation. Ps3 is positioned below Col2. On the west wall, at H:14–16.5, the truncation-like geometry of the north end of Col2 and the contact between Ps2a and Ps3 suggests that there is an unconformity present here that may have been caused by a small channel.

Ps3 abuts the fault on the east wall and shows little evidence of ductile deformation. In contrast, on the west wall, this paleosol abuts Cola where a finger of the unit appears to have been dragged up by the fault. There is a layer with abundant, large chunks of charcoal (designated as concentrated charcoal layer [CC1]) contained within Ps3. This charcoal probably came from a fire or a downed tree in the catchment area.

A package of colluviums (Col3a–d) is exposed below Ps3 and locally under CC1. Despite differences in descriptions between Col3a and Col3c in the east wall and between Col3b and Col3d in the west wall, we interpret them as being stratigraphically equivalent. All of the colluvium units in this package thin away from the fault, although the northern end of unit Col3d is truncated by Ps3 at approximately H:13.5 m on the west wall creating an angular unconformity. This package of colluvium is separated from an underlying package of colluvium by an angular unconformity at ~H:10.2 on the lower west wall. Below Col3d, all of the units slope down to the south, except near the fault zone where the units generally become more horizontal.

Another package of colluvium units that have different geometries on either side of the trench is exposed below Col3c and Col3d on the east and west walls, respectively. Col4a and Col4c form wedge-shaped deposits suggesting a fault scarp origin and Col4b forms a lens on the west wall. Col4c and Col4d are present on both walls and are of relatively uniform thickness. However, Col4d is truncated by Ps3 at ~H:14 on the lower west wall, forming another angular unconformity. The base of Col4d is generally obscure, except above charcoal-rich (Cr) layer 1, which is rich in charcoal fragments.

Cr1 is a lens-shaped deposit that clearly dips down to the south toward the fault, where it has been deformed and tilts gently to the north on both trench walls. Package Col5a underlies Cr1 and package Col4 and thins away from the fault.

Cr2 underlies Col5b on the east wall while on the west wall Ps4 underlies Col5a. Because Cr2 and Ps4 are stratigraphically equivalent, we think this provides evidence that locally units with abundant charcoal (i.e., CC1 and Cr1) may have a genesis similar to the units designated as paleosols. The difference in appearance between normal paleosols and the charcoal-rich layers could be due to variable leaching of the soil or because Ps4 formed in a localized depression that held more vegetation and allowed the concentration of organics. Ps4 is quite deformed (assuming it had a simple original

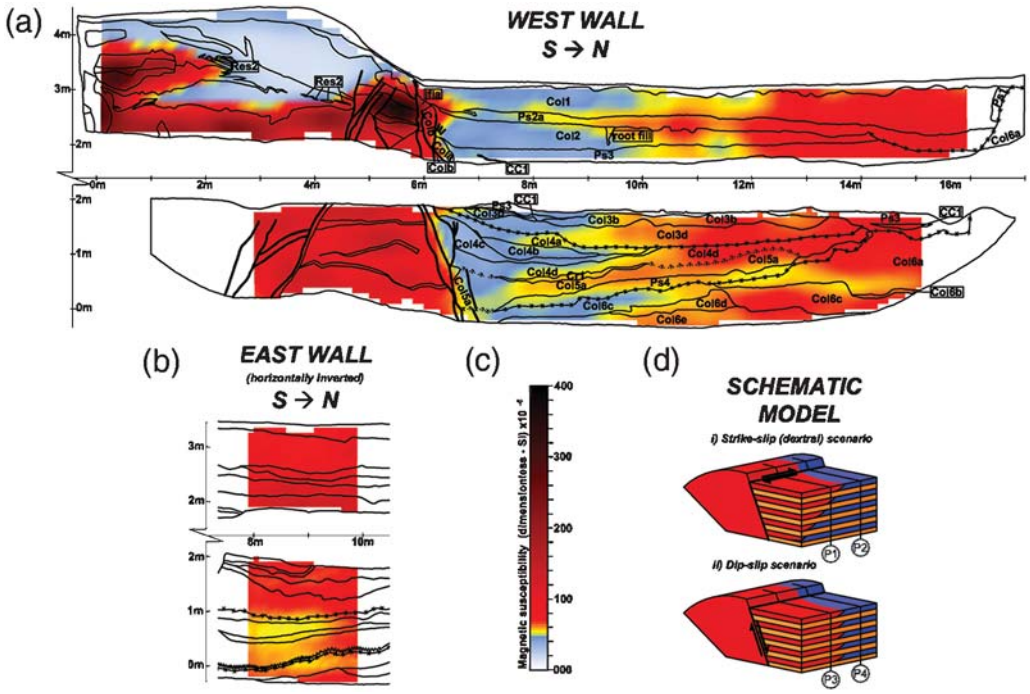

Figure 7. (a and b) Distribution of magnetic susceptibility (MS) on the trench walls overlain by unit boundaries from conventional paleoseismic trench log data (Fig. 5). Benches are depicted by vertical gaps. Panel C is the color scale of the MS data. Panel D shows two scenarios involving different faulting styles. In both scenarios the colors crudely reflect that of the MS data; blue equals low MS, red/orange equals medium to high MS. The scenario involves 5 phases of soil sourced from the upthrown side of the fault (red and blue) deposited on soil sourced from the adjacent slope (orange). The lines labeled P1 through P4 indicate profiles which are compared to the MS logs (panels A and B). The west wall MS log could be caused by strike-slip or dip-slip faulting (i.e., P2 or P4) but the east wall log can only be formed by a predominantly dip-slip scenario (i.e., P3 not P1).

geometry) and is truncated by Ps3. Ps4 dips down to the south toward the fault, but we did not observe any evidence for increased deformation closer to the fault. Cr2 also dips down toward the fault although near the fault zone it dips slightly to the north. The top of Cr2 is gradational south of H:11.5. The bases of Cr2 and Ps4 are interpreted as unconformities as Ps4 rests on an angular unconformity with package Col6. This unconformity is the oldest identified in the trench stratigraphy, and it is considered to be an irregular erosional contact. It also appears to have been truncated by a subsequent unconformity at the base of Ps3 at approximately H:14.5, V:15 on the lower west wall.

Col6 on the west wall and Col7 on the east wall are exposed beneath Ps4 and Cr2, respectively. These units are interpreted to be equivalent; however, the absence of an equivalent underlying paleosol unit makes this correlation uncertain. The individual colluviums within each of these packages interfinger, and some units thin to the north (scarp derived?) whereas others thin toward the fault (slope derived?). The base of the colluvium package on the east wall overlies Ps5 but is not exposed on the west wall. The top of Ps5 is wavy and dips toward the fault, probably reflecting postdepositional deformation.

Finally, Cola, Colb, and Cole are not assigned to specific packages of colluvium because they are associated with fault splays. The general homogeneity of the colluvial units makes it impossible to relate Cola, Colb, and Cole to the more continuous colluvial units to the north of the fault zone.

Magnetic Susceptibility

South of the fault zone, the distribution of magnetic susceptibility (MS) values clearly shows differences in the magnetic properties between exposed rock and overlying residual soil (Fig. 7a). The top of the rock unit has very high MS values, ranging from $\sim 100 \times 10^{-6}$ SI to 400×10^{-6} SI, compared to both the overlying residual soil and base of the rock unit. The different values likely reflect normal pedogenic processes that leach iron minerals from the residual soil and enrich the upper portion of the rock unit. MS values of the lower areas of exposed rock south of the fault, which are not significantly weathered, reflect the background MS value of the local rock.

North of the fault, wedges of low MS values thin away from the fault and are intercalated with wedges of higher MS values that thin toward the fault. We interpret that the low MS wedge units are derived from the residual soil on the upthrown side of the fault because of similar MS values and the wedge-shape geometry. We, therefore, interpret that these constitute colluvial wedges formed by failure of the fault scarp following earthquake events. These wedges were not recognized using conventional paleoseismic trench logging

techniques but provide a link between the deposition of the colluvial packages and fault rupture. The intercalated units with higher MS values are interpreted to be derived from the small unchannelized catchment area to the north. These units retain relatively high MS values, which suggest that the sediments are eroded, transported, and deposited without being entirely leached of iron minerals. The MS data strongly suggest that at the same time as the fault scarp collapses to form a colluvial wedge, coluvium from the slope to the north of the fault, which is visually undistinguishable from the colluvial wedge, is also deposited in the sediment trap.

The slope angle and length of exposed ground above each position appear to be key factors in determining the type of weathering on either side of the fault. In the small catchment area north of the trench, for example, the slope is relatively long and steep, which promotes physical erosion and transportation by overland flow. In contrast, atop the pop-up structure south of the fault, there is no slope other than the scarp. The accumulated residual soil indicates that physical erosion is minimal, and weathering largely occurs via chemical processes. Chemical weathering in the absence of physical weathering allows the iron minerals to be transported down the soil profile by infiltration. It is important to note that the leaching that occurs on the upthrown south side of the fault could also occur on the downthrown side of the fault, which would cause some downward migration of the wedge-shaped anomalies. However, the higher clay content and absence of fabric that characterizes the residual soil on the south side of the fault, leads to lower permeability and therefore, a lower rate of leaching processes on the downthrown side. In this case, the distribution of MS is critical to establishing the sequence stratigraphy genesis model, but the actual distribution of the MS is not as reliable as the conventional logging for constraining the location of event horizons.

Figure 7b is a 2 m wide swath log of MS H:7.9–9.9 of the east wall of the trench. The log has very little variation relative to the west wall log. This observation gives some insight into the style of faulting on the trenched fault strand and is discussed further in the Style of Faulting section.

Event Stratigraphy and Chronology

We created a sequence stratigraphy genesis model (Fig. 8) based on the patterns of sedimentation revealed by paleoseismic trench logging (Fig. 5 and 6) and MS logging (Fig. 7). During seismic quiescence, relatively organic-rich soil accumulates in the sediment trap due to the stability of the fault scarp and of the adjacent slope (Fig. 8a). Following a fault rupture, the scarp becomes unstable, ultimately failing and burying the local topsoil to form a colluvial wedge (Fig. 8b). This process is evidenced by the wedges of low MS soil that thin to the north in the MS data. This is accompanied by an increase in the rate of colluviation in the sediment trap as a result of increased erosion of the slope to the north of the trench site. Notably, the colluvium sourced from the fault scarp is visually indistinguishable from the colluvium sourced from the catchment area. Because the higher rate of sedimentation from the catchment area is coincident with colluvial wedge formation (i.e., fault scarp failure) we attribute this catchment area response to the earthquake (Fig. 8c). The increase in sediment flux may be

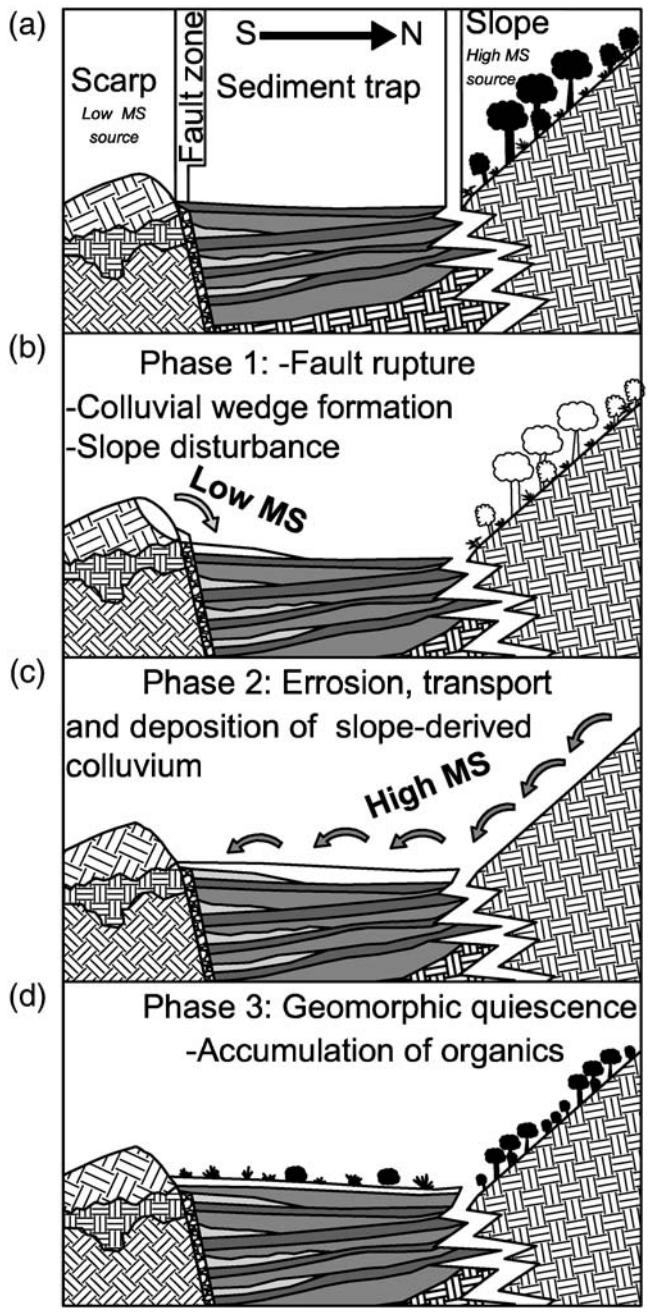

Figure 8. Interpretive model of sequence stratigraphy genesis. Panel A shows the three key zones involved in creating the stratigraphy exposed in Destek trench. Panels B–D show the phases of sedimentation associated with a seismic cycle. Pedogenic processes occur throughout all phases of the model. During the first phase we think the earthquake significantly reduces the slope stability (discussed in the text) resulting in erosion and deposition in the second phase.

due to one factor or a combination of factors. Seismically triggered tree fall, tree damage, or tree mortality in the catchment area to the north of the trench could increase the overland flow during rainfall events, leading to increased erosion and transportation. After large earthquake events near population centers, the increased demand for construction materials could lead to localized deforestation. In our case, we favor the concept of "shattered landscapes" proposed by Keefer and Moseley (2004), which involves "abundant landslides, pervasive ground cracking, microfracturing of surficial hillslope materials, collapse of drainage banks, widening of hillside rills. . ." in response to ground shaking. A shattered landscape in conjunction with overland flow would deposit a relatively homogenous package of colluvium, like those we observed in the sediment trap.

After a ground-rupturing earthquake event and the associated geomorphic response of local landscapes, surface stability is reestablished, and rates of colluvium deposition in the sediment trap are reduced, allowing the accumulation of organics and the formation of organic-rich paleosols (Fig. 8d). In all, the cycle of geomorphic quiescence and activity related to the cyclic deposits of paleosols and colluvium can be attributed to seismic quiescence and seismic activity. Therefore, the moment in time when geomorphic quiescence is disturbed by fault rupture is represented in the stratigraphic record as the top of the paleosol packages (or equivalent evidence for geomorphic quiescence) and base of overlying colluvial packages, which we refer to as an event horizon (EH).

We have identified at least seven event horizons (EH1–7) at Destek (Fig. 9). To constrain the timing of the paleoearthquakes we used the most reliable dates from above and below the event horizons, which were selected based on their stratigraphic position, sample type, size, yield, and observations made during laboratory processing (Appendix B, Tables A1 and 2). Sample 51b, consisting of the b portion of the sample, is considered to be a reliable age but is out of stratigraphic order; therefore, it is considered to be reworked. Sample 257 is also out of stratigraphic order, which we also attribute to reworking. While the gastropods appear to provide accurate dates, their precision is very poor due to the error incorporated by establishing a correction from a small dataset (Appendix B, Table A1). We, therefore, do not use the gastropod ages because the dates provided by the charcoal provide more accurate constraints on earthquake timing. The OxCal model (Ⓔavailable in the electronic edition of *BSSA*) that we used to model the age of samples and paleoearthquakes has an overall agreement index (Amodel) of 105 (Fig. 10).

The evidence for the youngest two events, E0 and E1, is quite complicated. On the east wall at ~H:6.5 (Fig. 6a) Ps2b has collapsed into the fault zone (reflected in the downward folding of Ps2b) and overlies fissure fill (Ifl) B, which suggests that this fissure fill was deposited at the same time as the event that caused at least part of this deformation. IflC and IflB, on the lower and upper east wall, respectively, are interpreted as the same unit separated by the bench, and they are

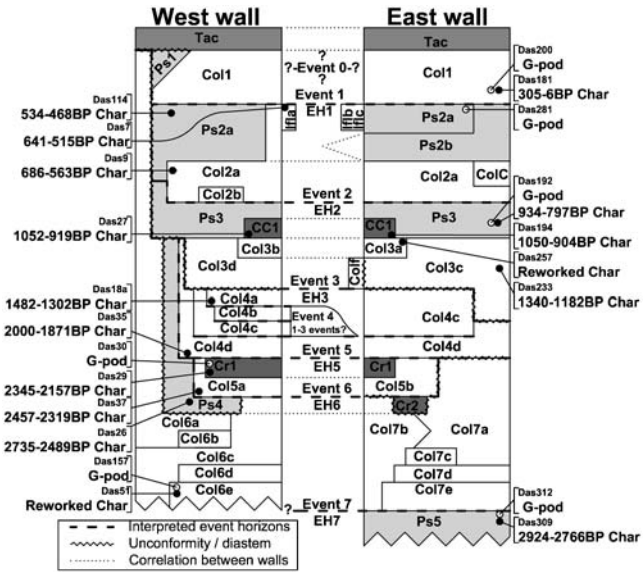

Figure 9. Generalized stratigraphic column showing event horizons 1–7 that are exposed in the Destek trench. Ages that constrain the timing of the events are given in calendar years B.P. ($\pm 1\sigma$) (see text for details).

stratigraphically equivalent to IflA exposed on the upper west wall. The top of IflA is coincident with the top of Ps2a, and the southern side of the unit appears to have been sheared upward, which indicates that another event has occurred since it was deposited. A small piece of Ps2b (labeled Ps7) has been offset by 15 cm at ~H:6.1 (Fig. 6a), and the fault extends into coluvium Col1. Therefore, the ultimate event (E0) occurred when at least part of coluvium Col1 had been deposited, and the penultimate event (E1) occurred when Ps2a was at the surface and resulted in deposition of IflA–C. We have not identified an event horizon associated with E0 and have not dated any samples to constrain its age, but we are convinced that E0 was the historical 1943 Tosya earthquake.

E1 is evidenced by event horizon (EH)1, which is defined in our stratigraphic record as the base of Col1 and the tops of Ps2a and Ps2b. On the west wall of the trench the magnetic susceptibility data (Fig. 7a) clearly show a wedge of low MS material that thins to the north away from the fault; we think this is a reliable definition of a colluvial wedge. As discussed in the previous paragraph, IflA–C were deposited during this event and Ps2b collapsed on top of IflB. The age of E1 is constrained by sample Das181a (as the A fraction is generally considered to be more reliable than the B fraction) from Col1 on the east wall of the trench and Das114 from Ps2a for the west wall of the trench, which has a relatively similar age to Das7 from IflA. There is a 95% probability that E1 occurred between A.D. 1437 and 1788 (Fig. 10, Table 2).

E2 is evidenced by EH2, which is defined as the base of Col2 and the top of Ps3. Col2 thins away from the fault; however, the volume of the wedge is far too great to have been sourced from fault scarp collapse (Fig. 5a). We clearly

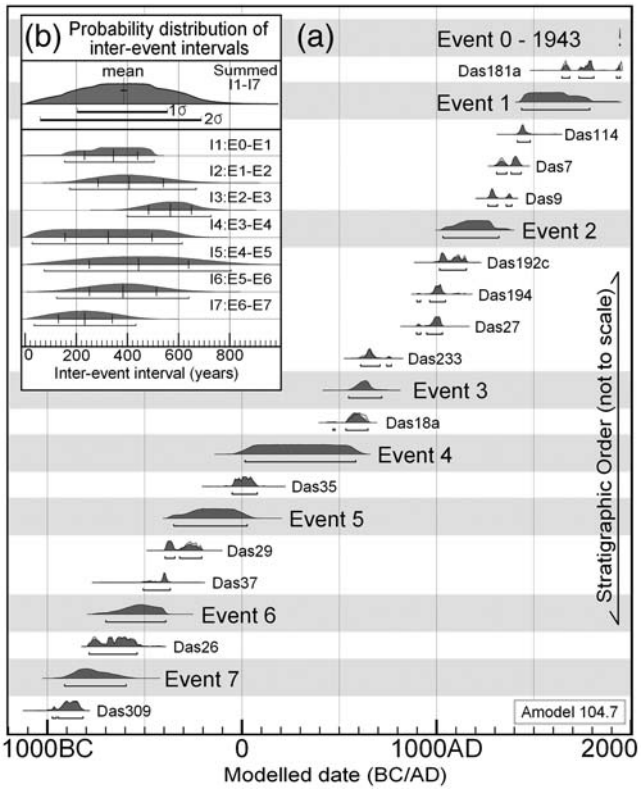

Figure 10. (a) Chronological model created by OxCal (see Data and Resources section) using a script Ⓔ available in the electronic edition of *BSSA*. This plot shows the probability distribution functions of the age of selected samples, which are determined by calibration using IntCal04 atmospheric curve (Reimer *et al.*, 2004) of measured radiocarbon ages. The data are arranged in stratigraphic order vertically. Prior calibrated radiocarbon age distributions are presented as open curves, posterior distributions are shown by filled curves, and black lines below the x axis show the extent of the 2σ standard deviation. Corresponding sample numbers are adjacent to each distribution. Modeled distributions of earthquake ages for E0–E7 are highlighted by gray shading. Table 2 contains the numerical details of this plot. The overall agreement index for this model is 105, which is very positive. (b) Shows the interevent intervals determined using the OxCal model. The summed interevent interval probability distribution function describes the average time between earthquakes [385(mean) $\pm$ 166(1σ)].

recognize an MS colluvial wedge associated with this event (Fig. 7a), which indicates that part of Col2 is derived from the fault scarp, and the remainder is from the catchment area north of the trench. The age of E2 is constrained by samples Das9 from Col2 on the west wall and Das192 from Ps3 on the east wall. There is a 95% probability that E2 occurred between A.D. 1034 and 1321 (Fig. 10, Table 2).

E3 is evidenced by event horizon EH3, which is defined as the bases of Col3d and Col3c on the west and east walls, respectively. On the west wall, Col4a, which underlies event horizon EH3, has an MS signature of scarp derived colluvium near the fault and an MS signature of catchment area derived colluvium north of ~H:8. Col3d, above the event horizon, has a low MS, which extends much further north indicating that when it was being deposited, there was an influx of scarp derived sediment. Additionally, an angular unconformity between truncated Col4c and the overlying Col3d at H:10.2 on the bottom west wall indicates that erosion was occurring prior to the deposition of sediments above EH3. Resumption of colluviation and an influx of scarp derived sediments are attributed to earthquake event E3. The age of E3 is constrained by samples Das233 from Col3 on the east wall and Das18a from Col4a on the west wall. This is the same sample that constrains the minimum age of the E4, so we have poor resolution between these events. There is a 95% probability that E3 occurred between A.D. 549 and 719 (Fig. 10, Table 2).

E4 is a little more complicated than the other events. We are unsure if we have constrained the age of 1, 2, or 3 events. Our discussion focuses on the west wall as the relative strata is not present on the east wall of the trench (Fig. 5). Col4a has a colluvial wedge-shaped geometry (Fig. 5); however, Figure 7a demonstrates that it has a relatively high MS, which means that this is probably not a colluvial wedge. Col4b and Col4c have distinctly low MS, which along with their geometries suggests they are scarp derived (Fig. 7a). Because Col4b and Col4c are in contact, they may be part of the same colluvial wedge. Col4d has a low MS near the fault, but over much of its extent it has a medium MS, which suggests that it is predominantly sourced from the catchment area with less of a contribution from scarp derived low MS soils. On the west wall there are two notable fault terminations below the top of Col4c (Fig. 6B). The MS data suggest that there is an event horizon at the base of Col4c, while the fault terminations suggest that there is an event horizon at the top of Col4c. Furthermore, the wedge-shaped geometry of Col4a, Col4b, and Col4c suggesst that their bases may all be event horizons. The samples that constrain the age of these 1–3 event horizons constituting E4 are Das18a from Col4a and Das35 from Col4d. There is a 95% probability that E4 occurred between A.D. 17 and 585 (Fig. 10, Table 2).

E5 is evidenced by event horizon EH5, which is defined as the base of Col4d and the top of Cr1. Although Cr1 is not a paleosol, it is interpreted to have a similar origin based on a correlation made in the North of the Fault Zone section. Therefore, the deposition of Col4d on top of Cr1 represents resumption of geomorphic activity following a period of geomorphic quiescence. On the west wall we recognize two conspicuous upward fault terminations at about EH5 (Fig. 6B, H:6.5 V:0.5). The MS data are vague in this part of the trench; the low MS material near the fault zone may be a consequence of increased downward migration of iron minerals near the fault zone. The age of E5 is constrained by samples Das35 from Col4d and Das29 from Cr1; both samples are from the west wall. There is a 95% probability that E5 occurred between 351 B.C. and A.D. 28 (Fig. 10, Table 2).

E6 is evidenced by event horizon EH6, which is defined as the base of Col5a and the top of Ps4 on the lower west wall. We interpret Col5a and Ps4 on the east wall to be stratigraphically equivalent to Col5b and Cr2 on the west wall,

Table 2

Summary of ^{14}C Results Constraining E1–7 at Destek

Sample Number	Soil unit[§]	Trench Wall	Lab Number	AMS Number	Material	Mass (mg)	$\delta^{13}C$	^{14}C Activity	^{14}C (yr B.P.)[*]		Calibrated Age (yr B.P.)[†]	
								Unrounded	Unrounded	Rounded[‖]	Unmodeled	Modeled
1943 Tosya Earthquake (E0)												
Das-181a	Col1	E	DL-407	AA-75205	Charcoal (A)	1194	−24.5	0.9740 ± 0.0036	212 ± 30	210 ± 30	305 – 4	305 – 6
E1 Occurred between 513 and 162 yr B.P. (2σ); There Is a 95% Probability That E1 Occurred between A.D. 1437 and 1788												
Das-114	Ps2a	W	DL-405	AA-75204	Charcoal (A)	1240	−24.9	0.9460 ± 0.0035	446 ± 30	450 ± 30	535 – 464	534 – 468
Das-7	Ifla	W	DL-451	AA-76609	Charcoal (A)	484	−25 [‡]	0.9336 ± 0.0041	552 ± 36	550 ± 35	644 – 515	641 – 515
Das-9	Col2	W	DL-452	AA-76610	Charcoal (A)	1024	−24.8	0.9175 ± 0.0036	692 ± 31	690 ± 30	686 – 562	686 – 563
E2 Occurred between 917 and 629 yr B.P. (2σ); There Is a 95% Probability That E2 Occurred between A.D. 1034 and 1321												
Das-192c	Ps3	E	DL-460	AA-76618	Charcoal (A)	996	−24.5	0.8859 ± 0.0034	973 ± 31	970 ± 30	935 – 794	934 – 797
Das-194	CC1	E	DL-461	AA-76619	Charcoal (A)	1036	−24.1	0.8808 ± 0.0034	1019 ± 31	1020 ± 30	1048 – 802	1050 – 904
Das-27	CC1	W	DL-455	AA-76613	Charcoal (A)	857	−24.7	0.8786 ± 0.0034	1040 ± 31	1040 ± 30	1053 – 917	1052 – 919
Das-257	Col3a	E	DL-463	AA-76621	Charcoal (A)	621	−25[‡]	0.8295 ± 0.0045	1502 ± 44	1500 ± 40	1518 – 1307	REWORKED
Das-233	Col3c	E	DL-462	AA-76620	Charcoal (A)	972	−24.9	0.8427 ± 0.0038	1375 ± 37	1370 ± 40	1354 – 1185	1340 – 1182
E3 Occurred between 1401 and 1231 yr B.P. (2σ); There Is a 95% Probability That E3 Occurred between A.D. 549 and 719												
Das-18a	Col4a	W	DL-453	AA-76611	Charcoal (A)	1234	−24.7	0.8335 ± 0.0036	1463 ± 35	1460 ± 30	1406 – 1301	1482 – 1302
E4 (Possibly More Than One Event) Occurred between 1934 and 1365 yr B.P. (2σ); There is a 95% Probability That E4 Occurred between A.D. 17 and 585												
Das-35	Col4d	W	DL-458	AA-76616	Charcoal (A)	1027	−24.5	0.7807 ± 0.0031	1988 ± 32	1990 ± 30	2001 – 1871	2000 – 1871
E5 Occurred between 2300 and 1923 yr B.P. (2σ); There Is a 95% Probability That E5 Occurred between 351 B.P. and A.D. 28												
Das-29	Cr1	W	DL-457	AA-76615	Charcoal (A)	859	−23.8	0.7553 ± 0.0031	2255 ± 33	2250 ± 30	2345 – 2155	2345 – 2157
Das-37	Col5a	W	DL-459	AA-76617	Charcoal (A)	1048	−24.1	0.7471 ± 0.0033	2342 ± 35	2340 ± 40	2482 – 2210	2457 – 2319
E6 Occurred between 2649 and 2341 yr B.P. (2σ); There Is a 95% Probability That E6 Occurred between 700 and 392 B.C.												
Das-26	Ps4	W	DL-456	AA-76614	Charcoal (A)	1426	−24.7	0.7314 ± 0.0030	2512 ± 33	2510 ± 30	2740 – 2471	2735 – 2489
Das-51	Col6e	W	DL-404	AA-76622	Charcoal (A)	248	−25[‡]	0.6894 ± 0.0039	2987 ± 45	2990 ± 50	3332 – 3005	REWORKED
E7 Occurred between 2861 and 2545 yr B.P. (2σ); There Is a 95% Probability That E7 Occurred between 912 and 596 B.C.												
Das-309	Ps5	E	DL-409	AA-75207	Charcoal (A)	1227	−23.9	0.7103 ± 0.0028	2748 ± 32	2750 ± 30	2925 – 2667	2924 – 2766

[*]Uncertainties for unrounded and rounded ^{14}C ages are given at the 1σ (68.3%) confidence level.

[†]Unmodeled and modeled calibrated ages are determined using OxCal (see Data and Resources section).
Unmodeled and modeled calibrated ages are given at the 2σ (95.4%) confidence level.
Ages are calibrated with the Incal04 curve.
Ages presented are the bounds of 2σ standard deviation distribution.

[‡]$\delta^{13}C$ value not measured.

[§]The soil unit refers to unit labels in trench log figures and descriptions in Appendix C.

[‖]Rounding follows convention (Stuiver and Polach, 1977).
Modeled calibrated ages from the OxCal model are used to constrain the timing of earthquake events.

respectively. Therefore, Cr2 also represents a period of low geomorphic activity, which by correlation, supports the interpretation for event horizon EH5 in the previous paragraph. There is an ~10 cm horizontal step of a subvertical fault (Fig. 6B, H:6.8 V:0), which correlates to the event horizon. Near the fault zone MS values of Col5a are low, which is consistent with a scarp source for part of the colluvium; however, this may be a result of the movement of iron minerals near the fault zone. In contrast with the MS data, the geometry of Col5a is wedge-shaped, thinning away from the fault (on both walls), which suggests a fault scarp origin. The interevent time between events E6 and E7 (I7, Fig. 10) is uncharacteristically short (233 ± 105 yr, 1σ), which may have resulted in a smaller accumulation of low MS soil on the upthrown side of the fault prior to fault rupture and, therefore, provided less low MS material for the colluvial wedge. The age of E6 is constrained by samples Das37 from Col5a on the west wall and Das26 from Ps5 on the west wall. There is a 95% probability that E6 occurred between 700 and 392 B.C. (Fig. 10, Table 2).

E7 is evidenced by event horizon EH7, which is defined on the east wall at the top of Ps5 but is not exposed on the west wall. The distinctive change in sedimentation from Ps5 to package Col7 on the east wall, which is equivalent to package Col6 on the west wall, indicates an earthquake has occurred. On the west wall Col6e has a low MS near the fault, although we only have a small amount of data. Above Col6e, Col6c has a distinctively low MS indicating a scarp source for this unit; we think this was a later phase of scarp failure. The age of E7 is constrained by samples Das26 from Ps4 on the west wall and Das309 from Ps5 on the east wall. There is a 95% probability that E7 occurred between 912 and 596 B.C. (Fig. 10, Table 2).

We also used a hand auger to examine sediments to a depth of ~1 m below the base of our trench and encountered two additional paleosols. We had to abandon the holes due to the presence of large gravel clasts, but information related to event horizons older than E7 are present in the sediments below the limit of our investigation.

Discussion

Style of Faulting

Remembering that we have trenched a splay (f3, Figs. 3 and 4) off the main strand of the dextral strike-slip NAF (f1, Figs. 3 and 4), we think that the MS data provide strong evidence to suggest that this splay undergoes predominantly dip-slip displacements. The northern edge of the f3 fault zone (Figs. 3 and 4), which bounds the sediment trap, dips at ~70° to the north (Figs. 5–7). On this splay of the fault we did not recognize any geomorphological or geological piercing points, which indicate strike-slip displacement, but there is a clear displacement down to the north. On the west wall we have recognized a sequence of wedge-shaped magnetic anomalies on the northern, downthrown side of the fault. We think these low MS wedges came from residual soils with very similar MS values exposed on the southern, upthrown side of the fault. Although we only logged a 2 m wide swath (H:7.9–9.9) of the east wall, we do not see the wedge-shaped deposits (Fig. 7b). In the conventional trench log we described residual soil south of the fault on the west wall while on the east wall, there was no residual soil. This residual soil has a low MS while the weathered rock has a medium to high MS similar to that of the weathered rock south of the fault on the lower west wall (Fig. 7a). Figure 7d is a schematic model of this situation where we see red, high MS rock and blue, low MS soil on the upthrown side of the fault. The sedimentary packages on the downthrown side of the fault reflect cyclic interfingering sedimentation sourced from the fault scarp (red and blue units) and the catchment area (orange). Because the NAF system is dextral, if this fault splay had a strike-slip component, it would also be dextral. Profiles P2 and P4 (Fig. 7d) are equivalent to the west wall MS log (Fig. 7a) where wedges of the blue low MS soils are deposited in the sediment trap. However, the absence of the blue low MS soils on the east wall MS log (Fig. 7b) means that the east wall is equivalent to P3 rather than P1. Therefore, because we do not see wedges of low MS on the MS log of the east wall, and we see a long record of wedges on the west wall, the deposits north of the fault have not moved laterally. We think this strongly indicates that this fault splay has undergone less than ~3 m of dextral strike-slip displacement. This is consistent with analog sand box models of restraining structures on strike-slip faults, which suggest that the bounding faults often undergo predominantly dip-slip displacement (McClay and Bonora, 2001).

Event Timing Relative to Other Studies

The 1943 Tosya earthquake ruptured a nearly 280 km stretch of the NAF, including the fault section in our study area (Barka, 1996), but evidence of this event is different from older events in the Destek trench. For some reason there was no paleosol formation between the penultimate and ultimate (1943) events that ruptured the trenched fault (f3) strand. We are also unable to distinguish the events, E1 from E0, in the MS data (Fig. 7), which suggests that either material was constantly being eroded (at a low rate) from the scarp over this period that there was some erosion of the sediments in the trap, or that these events occurred closely spaced in time. The ultimate–penultimate interevent time was shorter than the older interevent times but not considerably; therefore, the interevent time alone does not account for the lack of evidence for the 1943 earthquake. The absence of the paleosol may also reflect changes in local climate patterns, land use (e.g., deforestation or increased plowing), or vegetation cover. Barka (1996) described right-lateral offsets in the range 1.7–2.3 m and a vertical offset of 0.4–0.5 m (south up) in the vicinity of this study after the 1943 Tosya earthquake. If the seven earthquakes identified in our trench over the last 2700 yr caused an offset of 2.3 m, like the 1943

Tosya earthquake, the combined displacement would be 16.1 m, which corresponds to a slip rate of ~6 mm/yr. This slip rate is considerably lower than estimates of 20.5± 5 mm/yr determined from offset 2–2.5 ka old geomorphic features (Kozaci *et al.*, 2007) and GPS based estimates of 25.8 ± 0.2 mm/yr. The seven earthquakes identified over a 2700 yr period would need an average displacement per event of about 7.7 m to attain a slip rate of 20 mm/yr. It is possible that the Ezinepazari fault, a splay to the south from the Niksar pull-apart basin, may accommodate some of the plate boundary strain, but it is unlikely to cause such a significant reduction in slip rate on this fault strand. There is no evidence to suggest that this segment of the fault undergoes creep. Therefore, we infer that the 1943 Tosya earthquake involved an anomalously small fault rupture relative to the other events identified in this study and that this is why the 1943 earthquake is not evidenced in the stratigraphy like the preceding earthquakes. It is, therefore, possible that our earthquake chronology is missing events that caused displacements similar to the 1943 Tosya earthquake.

Findings in this study indicate that ground-rupturing earthquake E1 occurred during the period A.D. 1437 to 1788. Paleoseismic studies at Alayurt (Hartleb *et al.*, 2003) and Ilgaz (Sugai *et al.*, 1999) identified paleoseismic event windows between A.D. 1327–1943 and 1495–1850, respectively. These temporal windows all correlate with the historical A.D. 1668 earthquake (Ambraseys and Jackson, 1998; Sugai *et al.* 1999; Hartleb *et al.*, 2003), but it is possible that E1 in this study may correlate to an A.D. 1598 event recorded at Amasya (Ambraseys and Finkel, 1995). Both of these events are associated with a temporal cluster of earthquakes between the sixteenth and eighteenth centuries A.D. (Table 1, cluster 3). Sample Das114 was collected from quite deep within Ps2a below the event horizon while sample Das181 was collected just above the event horizon in Col1 suggesting that E1 is more probable later in the temporal window; therefore, we think E1 was the A.D. 1668 earthquake.

E2 occurred between A.D. 1034 and 1321. Paleoseismic studies at Alayurt (Hartleb *et al.*, 2003) and Ilgaz (Sugai *et al.*, 1999) identified events at A.D. 782–1401 (probably 782–1213) and 890–1190, respectively, which may reflect the same event or almost certainly the same seismic cycle. This temporal window does not directly correlate to a local historical event. The new data from this study corroborate a suggestion by Hartleb *et al.* (2003) that these paleoseismic events may correlate with a period of high NAF seismicity based on historical earthquakes of A.D. 967, 1035, and 1050 near Gerede and A.D. 1043 and 1045 near Erzincan (Fig. 2, Table 1). Two paleoseismic events spanning A.D. 890–1490 and 880–1160 that were identified by Hartleb *et al.* (2006) in a paleoseismic trench at Cukurcimen may also correlate to this seismic cycle. If rupture patterns associated with this cycle were similar to the A.D. 1943 Tosya earthquake that ruptured through Ilgaz, Alayurt, and Destek, then E2 probably occurred during the period A.D. 1034–1190.

E3 occurred between A.D. 549 and 719. This event may correlate with paleoseismic event windows identified at Ilgaz (Sugai *et al.*, 1999), Havza (Yoshioka *et al.*, 2000), and Alayurt (Hartleb *et al.*, 2003), which span A.D. 640–810, 235–1044, and 390– ~ 1000, respectively. However, the events at Havza and Alayurt may also correlate to E4 in this study. E3 does not correlate to any historical events in the vicinity but may be part of a seismic cycle associated with historical events near Izmit between the mid eighth and tenth centuries A.D. (Table 1, cluster 7)

E4 occurred between A.D. 17 and 585, but as we determined in the Event Stratigraphy and Chronology section, it probably reflects the timing of one earthquake, it possibly reflects the timing of two earthquakes, and we cannot preclude that it may reflect the timing of three earthquakes. E4 may correlate to paleoseismic events identified at Havza (Yoshioka *et al.*, 2000) and Alayurt (Hartleb *et al.*, 2003), which may also correlate to E3 from this study. E4 may also correlate to another event identified at Alayurt ~1500 B.C. (maximum 3630 B.C.)–A.D. 338 (Hartleb *et al.*, 2003), but this event has very poor temporal constraint and, therefore, is not discussed further. A paleoseismic event at A.D. 250–550 identified at Cukurcimen (Hartleb *et al.*, 2006) may also correlate to the seismic cycle(s) associated with these possible events. Three historical earthquakes are known during the E4 temporal window: (1) An earthquake was reported near Amasya in A.D. 236 (Ambraseys and Jackson, 1998) that is interpreted to have been encountered at Alayurt in a paleoseismic event window (Hartleb *et al.*, 2003). (2) An earthquake was reported at Niksar in A.D. 499 (Ambraseys and Jackson, 1998). (3) An earthquake or series of earthquakes reported in Amasya and other nearby cities occurred at A.D. 523–543 (Guidoboni *et al.*, 1994). We cannot be sure if one, two, or three events occurred over this period, but our interpretation of the stratigaphy suggested that it is probable that there is only one event during this period.

E5 occurred between 351 B.C. and A.D. 28. This temporal window may correlate to paleoseismic event windows established at Alayurt (Hartleb *et al.*, 2003) and Ilgaz (Sugai*et al.*, 1999) that span from ~1500 B.C. (maximum 3630 B.C.) to A.D. 338 and 150, respectively. The paleoseismic events identified at Ilgaz and Destek during this period may correlate to the same earthquake cycle (Table 1, cluster 10) on the NAF and possibly the same rupture event. This cycle may also correlate to historical events to the west in A.D. 29, 69, 181, and 155 (Şengör *et al.*, 2005), which suggests an east-to-west rupture pattern at this time, similar to the twentieth century cycle.

We also identified two additional paleoseismic events, E6 and E7, which occurred during the periods 700–392 and 912–596 B.C., respectively. Historical information does not cover this period. Based on the summary maps of Guidoboni *et al.* (1994), the historical records over this period are limited to densely populated areas, such as Italy and along the Aegean Sea. Event E at Cukurcimen probably occurred between 350 and 110 B.C. (Hartleb *et al.*, 2006), which could correlate to

E5 or E6 in this study. E7 may correlate with the same seismic cycle as Event F from Cukurcimen (Hartleb *et al.*, 2006) at 1610–820 B.C. More paleoseismic and/or historical data are required for this period along the NAF to determine if these speculative relationships are real.

Using the OxCal model we determined a recurrence interval of 388 ± 12 yr (standard error) for this section of the North Anatolian fault by subtracting the age of the most recent event (1943) from the oldest event (E7) and dividing the result by the number of events (7). To be more representative of the probable period between earthquakes we summed the probability distribution functions from each interevent interval (i.e., accounting for the probability distribution of the event timing). The resulting probability distribution function (Fig. 10, top left) describes the average interevent time as 385 ± 166 (1σ) yr. The notable difference between the recurrence interval and the probability distribution function of summed interevent intervals is the greater error associated with the latter, which we consider to be more representative of our data set. This range is comparable to the interevent times of 210− < 700 yr determined at Cukurcimen (Hartleb *et al.*, 2006), 250− ≥ 800 yr at Alayurt (Hartleb *et al.*, 2003), 280–620 yr at Ilgaz (Sugai *et al.*, 1999), and a less certain estimate of 600–900 yr from Havza (Yoshioka *et al.*, 2000).

Paleoseismology

The Paphlagonian temporal seismic gap (PTSG) identified by Şengör *et al.* (2005) is well defined by historical earthquake data. But paleoseismic data from Alayurt (Hartleb *et al.*, 2003), Ilgaz (Sugai *et al.*, 1999), Destek (this study), and to a lesser degree, Havaza (Yoshioka *et al.*, 2000), suggest that the PTSG is more likely a feature of an incomplete historical record rather than a lack of seismic cycles. As previously mentioned, additional records are needed to substantiate this hypothesis.

The number of paleoseismic event windows revealed by paleoseismic investigations appears to increase to the east along the NAF (Fig. 2). Assuming it is not an artifact of the density of study areas, this phenomenon may be due to an increase in structural simplicity of the fault zone to the east, which favors the preservation of tectonic structures by maintaining faulted landscapes for longer periods of time. Complex strike-slip faulting, like that exhibited in western Turkey, may cause more fault splays with shorter life spans and, therefore, is not as well preserved in the geologic record.

Conclusions

Turkey has a long historical record of earthquakes, which is highly reliable over the last century but suffers from incomplete and contradictory evidence prior to that. To extend our knowledge of the temporal and spatial patterns of large, ground-rupturing earthquakes along the NAF, we applied a combination of conventional trench logging and MS logging to sediments exposed in a paleoseismic trench near Destek in northern Turkey. We have estimated the timing of seven ground-rupturing earthquake events using these techniques and recognized evidence of the most recent (1943 Tosya) earthquake. The paleoseismic trench evidence of the 1943 Tosya earthquake is more subtle than the evidence for the older seven events identified in this study. This suggests that the earthquake record determined in this study may be missing events of a similar size to the Tosya earthquake and that the segment of the fault usually produces much larger offsets per event. E1 occurred between A.D. 1437 and 1788 and probably correlates to a historical A.D. 1668 earthquake or possibly an earthquake in A.D. 1598 reported near Niksar. E2, which occurred between A.D. 1034 and 1321, correlates with earthquake events identified by paleoseismic investigations to the west at Ilgaz and Alayurt but not with any known historical earthquakes. E3 occurred between A.D. 549 and 719 and does not correlate to any known historical earthquakes but may correlate to paleoearthquakes identified to the west at Ilgaz, Havza, and Alayurt. E4 occurred between A.D. 17 and 585; however, our interpretation of the trench cannot preclude up to three events having occurred during this period. This event may correlate to paleoearthquakes identified at Havza and Alayurt and up to three historical events in A.D. 236, 499, or an earthquake or series of earthquakes at A.D. 523–543 that may have ruptured this strand of the fault. E5 occurred at between 351 B.C. and A.D. 28, which may correlate to paleoearthquakes identified at Ilgaz and Alayurt, but there are no historical earthquakes during this period. The oldest two paleoseismic events identified in the Destek trench, E6 (700–392 B.C.) and E7 (912–596 B.C.) occurred prior to historical records and are only tentatively comparable to results from Cukurcimen. Our results indicate that the average interevent time is 385 ± 166 (1σ) yr, which is similar to other estimates from paleoseismic studies on the NAF.

Sediments exposed in our trench revealed a cyclic pattern of sedimentation that resulted in repeated packages of paleosols and colluvium associated with multiple earthquakes on the NAF. Data from Destek and other sites along the NAF, in conjunction with the catalog of historical events, provide a long record of relatively equally spaced regular fault ruptures over time. Particularly east of Bolu, temporal groupings of earthquakes show a relatively simple pattern. As concluded by Hartleb *et al.* (2003, 2006) the NAF appears to behave relatively independently of other tectonic features, without stress interaction; therefore, its seismicity is controlled by the accumulation of elastic strain caused by tectonic forcing.

The PTSG identified by Şengör *et al.* (2005) defines an apparent paucity in seismic activity from the sixth to sixteenth centuries A.D. between Bolu and Refhiye that is well documented in the historical earthquake data. We found evidence in this study, including E2 and possibly E3, of significant seismic activity during this period. Additional evidence of activity at this time comes from paleoseismic data from Alayurt (Hartleb *et al.*, 2003), Ilgaz (Sugai *et al.*, 1999), and to a lesser degree, Havaza (Yoshioka *et al.*, 2000).

Together, these results suggest that the PTSG may be the result of an incomplete historical record rather than a lack of seismic activity.

Trench logging is a well-established technique for paleoseismic investigations but is limited by the type and style of sedimentary structures that are exposed at a given locality. MS logging reveals information that is often invisible to the naked eye, which may be critical when establishing the genesis of the trench stratigraphy and constraining the timing and style of displacement on a complex fault system. We suggest that other physical properties of soils and sediments could be logged and utilized to provide information regarding nonvisible changes in exposed stratigraphic sections in many different environments.

Finally, we used novel ^{14}C dating techniques, specifically the comparison of ^{14}C activities of base-soluble and base-insoluble fractions (Appendix B), to evaluate the reliability of our radiocarbon-based chronology. While this technique is well known to most geochronologists, it is not in widespread use because it requires specific knowledge of the sample material and chemical pretreatment techniques and requires additional costs to complete multiple (rather than single) accelerator mass spectrometry (AMS) measurements for a given sample. Our ^{14}C results indicate that the ^{14}C activity of contaminant carbon species (humic acids or humates) is indistinguishable from the ^{14}C activity of original sample carbon. Therefore, even if contaminant C species are present in our samples and survive pretreatment procedures, measured ^{14}C ages are still considered to be robust. This technique may prove useful to other paleoseismic studies in the area and to researchers using ^{14}C dating in terrestrial environments in general.

Data and Resources

All data used in this article came from published sources listed in the references. A computer program, OxCal version 4.0.5 radiocarbon calibration software, was used for radiocarbon calibration and Bayesian statistical modeling and was developed by C. Bronk Ramsey (http://c14.arch.ox.ac.uk/embed.php?File=oxcal.html, last accessed March 2009).

Acknowledgments

This work was carried out in the frame of the Marie Curie Excellence Grant Project *Understanding the Irregularity of Seismic Cycles: A Case Study in Turkey* (MEXT-CT-2005-025617: Seismic Cycles) centered at the Seismology Section of the Royal Observatory of Belgium whom we would like to thank for their support. We are grateful for the assistance of Erhan Altunel of Osmangazi University for assistance with logistics. We also thank Lynda Klasky and the staff at the Desert Laboratory for daily support and assistance and Jay Quade for supplying access to his laboratories. We would like to warmly thank the people and local authorities of Destek, the land owners at the trench site, and the people of Boraboy where we stayed during field work. Finally, we thank R. Heermance, D. Malmon, an anonymous reviewer, and particularly J. Lienkaemper for reviews of preliminary versions of the manuscript.

References

Ambraseys, N. N. (1970). Some characteristic features of the Anatolian fault zone, *Tectonophysics* **9,** 143–165.

Ambraseys, N. N. (2001). Reassessment of earthquakes, 1900–1999, in the Eastern Mediterranean and the Middle East, *Geophys. J. Int.* **145,** no. 2, 471–485.

Ambraseys, N. N., and C. Finkel (1995). *The Seismicity of Turkey and Adjacent Areas: A Historical Review, 1500–1800*, Muhittin Salih Eren, Istanbul, 0–240.

Ambraseys, N. N., and C. F. Finkel (1987). Seismicity of Turkey and neighbouring regions, 1899–1915, Annales geophysicae B, *Terr. Planet. Phys.* **5,** no. 6, 701–725.

Ambraseys, N. N., and J. Jackson (1998). Faulting associated with historical and recent earthquakes in the Eastern Mediterranean region, *Geophys. J. Int.* **133,** no. 2, 390–406.

Barka, A. A. (1996). Slip distribution along the North Anatolian fault associated with the large earthquakes of the period 1939 to 1967, *Bull. Seismol. Soc. Am.* **86,** no. 5, 1238–1254.

Barka, A. A., and P. L. Hancock (1984). Neotectonic deformation patterns in the convex-northwards arc of the North Anatolian fault zone, In *The Geological Evolution of the Eastern Mediterranean*, Geological Society of London, Special Publications **17,** 763–774.

Barka, A. A., and K. Kadinsky-Cade (1988). Strike-slip fault geometry in Turkey and its influence on earthquake activity, *Tectonics* **7,** no. 3, 663–684.

Barka, A. A., S. H. Akyüz, H. A. Cohen, and F. Watchorn (2000). Tectonic evolution of the Niksar and Tasova–Erbaa pull-apart basins, North Anatolian fault zone: Their significance for the motion of the Anatolian block, *Tectonophysics* **322,** 243–264.

Berrill, J. B. (1988). Diversion of faulting by hills, *Q. J. Eng. Geol.* **21,** 371–374.

Bozkurt, E. (2001). Neotectonics of Turkey—A synthesis, *Geodinamica Acta* **14,** 3–30.

Faccenna, C., O. Bellier, J. Martinod, C. Piromallo, and V. Regard (2006). Slab detachment beneath eastern Anatolia: A possible cause for the formation of the North Anatolian fault, *Earth Planet. Sci. Lett.* **242,** no. 1–2, 85–97.

Flerit, F., R. Armijo, G. King, and B. Meyer (2004). The mechanical interaction between the propagating North Anatolian Fault and the back-arc extension in the Aegean, *Earth Planet. Sci. Lett.* **224,** no. 3, 347–362.

Goodfriend, G. A., and J. J. Stipp (1983). Limestone and the problem of radiocarbon dating of land-snail shell carbonate, *Geology* **11,** no. 10, 575–577.

Guidoboni, E., and A. Comastri (2005). Catalogue of earthquakes and tsunamis in the mediterranean area from the 11th to the 15th century, Istituto Nazionale di Geophysical e Vulcanologia, Bologna, 1037.

Guidoboni, E., A. Comastri, and G. Traina (1994). *Catalogue of ancient earthquakes in the Mediterranean area up to the 10th century*, Istituto Nazionale di Geofisica, 504.

Hartleb, R., J. Dolan, H. Akyüz, and B. Yerli (2003). A 2000-year-long paleoseismologic record of earthquakes along the central North Anatolian fault, from trenches at Alayurt Turkey, *Bull. Seismol. Soc. Am.* **93,** no. 5, 1935–1954.

Hartleb, R., J. Dolan, O. Kozaci, H. Akyuz, and G. Seitz (2006). A 2500-yr-long paleoseismologic record of large, infrequent earthquakes on the North Anatolian fault at Cukurcimen Turkey, *Bull. Geol. Soc. Am.* **118,** no. 7–8, 823.

Hilley, G. E., and J. J. Young (2008). Deducing paleoearthquake timing and recurrence from paleoseismic data, Part I: Evaluation of New Bayesian Markov-Chain Monte Carlo simulation methods applied to excavations with continuous peat growth, *Bull. Seismol. Soc. Am.* **98,** no. 1, 383.

Hua, Q., and M. Barbetti (2004). Review of tropospheric bomb 14C data for carbon cycle modeling and age calibration purposes, *Radiocarbon* **43,** no. 3, 1273–1298.

Hubert-Ferrari, A., R. Armijo, G. King, B. Meyer, and A. Barka (2002). Morphology, displacement, and slip rates along the North Anatolian Fault Turkey, *J. Geophys. Res.* **107,** 2235.

Keefer, D. K., and M. E. Moseley (2004). Southern Peru desert shattered by the great 2001 earthquake: Implications for paleoseismic and paleo-El Nino-southern oscillation records, *Proc. of the National Academy of Sciences* 101**,** no. 30, 10878–10883.

Klinger, Y., K. Sieh, E. Altunel, A. Akoglu, A. Barka, T. Dawson, T. Gonzalez, A. Meltzner, and T. Rockwell (2003). Paleoseismic evidence of characteristic slip on the western segment of the North Anatolian fault Turkey, *Bull. Seismol. Soc. Am.* **93,** no. 6, 2317–2332.

Kondo, H., Y. Awata, O. Emre, A. Dogan, S. Ozalp, F. Tokay, C. Yildirim, T. Yoshioka, and K. Okumura (2005). Slip distribution, fault geometry, and fault segmentation of the 1944 Bolu-Gerede earthquake rupture, North Anatolian fault Turkey, *Bull. Seismol. Soc. Am.* **95,** no. 4, 1234–1249.

Kondo, H., V. Ozaksoy, c. Yildirim, Y. Awata, O. Emre, and K. Okumura (2003). 3D trenching survey at Demire Tepe site on the 1944 Bolu-Gerede earthquake ruptures, North Anatolian fault system, Turkey, *Seism. Res. Lett.* **75,** no. 2, 292.

Kozaci, O., J. F. Dolan, C. F. Finkel, and R. Hartleb (2007). Late Holocene slip rate for the North Anatolian fault, Turkey, from cosmogenic 36Cl geochronology: Implications for the constancy of fault loading and strain release rates, *Geology* **35,** no. 10, 867–870.

Kozaci, O., J. F. Dolan, and C. F. Finkel (2009). A late Holocene slip rate for the central North Anatolian fault, at Tahtakopru, Turkey, from cosmogenic ^{10}BE geochronology: Implications for fault loading and strain release rates, *J. Geophys. Res.* **114,** B01405.

Lettis, W., J. Bachhuber, R. Witter, C. Brankman, C. E. Randolph, A. Barka, W. D. Page, and A. Kaya (2002). Influence of releasing step-overs on surface fault rupture and fault segmentation: Examples from the 17 August 1999 Izmit earthquake on the North Anatolian fault Turkey, *Bull. Seismol. Soc. Am.* **92,** no. 1, 19–42.

McCalpin, J. (1996). *Paleoseismology*, in International Geophysics Series, J. McCalpin (Editor), Academic Press, San Diego, 583

McClay, K., and M. Bonora (2001). Analog models of restraining stepovers in strike-slip fault systems, *AAPG Bull.* **85,** no. 2, 233–260.

Okumura, K., T. Rockwell, T. Duman, F. Tokay, Y. Awata, H. Kondo, V. Ozaksoy, and C. Yildirim (2003). Refined slip history of the North Anatolian fault at Gerede on the 1944 rupture, *American Geophysical Union*, Fall Meeting 2003, Abstract S12B-0384.

Okumura, K., T. Yoshioka, and I. Kusçu (1994). Surface faulting on the North Anatolian fault in these two millennia, *Proc. of the Workshop on Paleoseismology*, *Open-File Rept. (94-568)*, 143–144.

Okumura, K., T. Yoshioka, I. Kuscu, H. Kayanne, and Y. Suzuki (1993). Recent surface faulting along the North Anatolian fault east of Erzincan Basin, Turkey—A trenching survey, *EOS Trans. Am. Geophys. Union* **74**, (Fall Meeting), F545.

Palyvos, N., D. Pantosti, C. Zabci, and G. D'Addezio (2007). Paleoseismological evidence of recent earthquakes on the 1967 Mudurnu Valley earthquake segment of the North Anatolian fault zone, *Bull. Seismol. Soc. Am.* **97,** no. 5, 1646–1661.

Pigati, J. S., J. Quade, T. M. Shahanan, and C. V. Haynes (2004). Radiocarbon dating of minute gastropods and new constraints on the timing of late quaternary spring-discharge deposits in southern Arizona, USA, *Palaeogeography, Palaeoclimatology, Palaeoecology* **204,** 33–45.

Pucci, S. (2006). The Duzce segment of the north Anatolian fault zone (Turkey): Understanding its seismogenic behavior through earthquake geology, tectonic geomorphology and paleoseismology, *PhD Thesis*, Universita degli studi di Perugia.

Reilinger, R., S. McClusky, P. Vernant, S. Lawrence, S. Ergintav, R. Cakmak, H. Ozener, F. Kadirov, I. Guliev, R. Stepanyan, M. Nadariya, G. Hahubia, S. Mahmoud, K. Sakr, A. ArRajehi, D. Paradissis, A. Al-Aydrus, M. Prilepin, T. Guseva, E. Evren, A. Dmitrotsa, S. V. Filikov, F. Gomez, R. Al-Ghazzi, and G. Karam (2006). GPS constraints on continental deformation in the Africa-Arabia-Eurasia continental collision zone and implications for the dynamics of plate interactions, *J. Geophys. Res.* **111,** 1–26.

Reimer, P. J., M. G. L. Baillie, E. Bard, A. Bayliss, J. W. Beck, C. J. H. Bertrand, P. G. Blackwell, C. E. Buck, G. S. Burr, K. B. Cutler, P. E. Damon, R. L. Edwards, R. G. Fairbanks, M. Friedrich, T. P. Guilderson, A. G. Hogg, K. A. Hughen, B. Kromer, F. G. McCormack, S. W. Manning, C. B. Ramsey, R. W. Reimer, S. Remmele, J. R. Southon, M. Stuiver, S. Talamo, F. W. Taylor, J. Van Der Plicht, and C. E. Weyhenmeyer (2004). IntCal04 terrestrial radiocarbon age calibration, 0–26 Ka cal BP, *Radiocarbon* **46,** no. 3, 1029–1058.

Rockwell, T. K., E. Aksoy, G. Ucarkus, A. Barka, D. Ragona, D. Dier, M. Ferry, Y. Klinger, R. Langridge, M. Meghraoui, A. Meltzner, and G. Seitz (2001). Results of paleoseismic studies after the 1999 Izmit earthquake: Implications for seismic hazard to Istanbul, *European Union of Geosciences meeting*, 2001, Strasbourg, Abstract 1, 292.

Rockwell, T., A. Barka, T. Dawson, S. Akyuz, and K. Thorup (2001). Paleoseismology of the Gazikoy-Saros segment of the North Anatolia fault, northwestern Turkey: Comparison of the historical and paleoseismic records, implications of regional seismic hazard, and models of earthquake recurrence, *J. Seismol.* **5,** no. 3, 433–448.

Şengör, A. M. C., and N. Canitez (1982). The North Anatolian Fault, in *Alpine-Mediterranean Geodynamics*, H. Berekhemer and K. Hsu (Editors), American Geophysics Union, Boulder, Colorado, **7,** 205–16.

Şengör, A. M. C., O. Tüysüz, C. Imren, M. Sakinç, H. Evidoğan, N. Görür, X. Le Pichon, and C. Rangin (2005). The North Anatolian fault: A new look, *Annu. Rev. Earth Planet. Sci.* **33,** no. 1, 37–112.

Slota, P. J., A. J. T. Jull, T. W. Linick, and L. J. Toolin (1987). Preparation of small samples for 14 C accelerator targets by catalytic reduction of CO, *Radiocarbon* **29,** no. 2, 303–6.

Stein, R. S., A. A. Barka, and J. H. Dieterich (1997). Progressive failure on the North Anatolian fault since 1939 by earthquake stress triggering, *Geophys. J. Int.* **128,** no. 3, 594–604.

Stuiver, M., and H. A. Polach (1977). Discussion: Reporting of 14 C data, in *Radiocarbon* **19,** 355–363.

Sugai, T., O. Emre, T. Duman, T. Yoshioka, and I. Kuscu (1999). Geologic evidence for five large earthquakes on the north Anatolian Fault at Ilgaz, during the last 2000 years —a result of GSJ—MTA international cooperative research, in *The Paleoseismology Workshop* K. Satake and D. Schwartz (Editors), *U.S. Geol. Surv. Open-File Rept. 99-400*, Japan, 66–72.

Wdowinski, S., Y. Bock, G. Baer, L. Prawirodirdjo, N. Bechor, S. Naaman, R. Knafo, Y. Forrai, and Y. Melzer (2004). GPS measurements of current crustal movements along the Dead Sea fault, *J. Geophys. Res.* **109,** 1–16.

Yoshioka, T., K. Okumura, I. Kuscu, and O. Emre (2000). Recent surface faulting of the North Anatolian fault along the 1943 Ladik earthquake ruptures, *Bull. Geol. Surv. Japan* **51,** no. 1, 29–36.

Appendix A

Magnetic Susceptibility Method

MS measurements were performed in a grid pattern on the west wall of the trench and a 2 m wide swath of the east wall to create two-dimensional logs of MS distribution (Fig. 7). Point measurements were made using a Bartington MS2E point sensor in vertical profiles with 5 cm spacing and profiles were horizontally spaced 20 cm apart. The sensory tip of the probe is composed of a circular surface with a diameter of 10.5 mm. The measurement is made from a rectangular area at the end of the probe that is 3.8 mm high and

10.5 mm wide. The long axis of the rectangular area was kept horizontal during field measurements. The sensitivity of the MS measurement decreases away from the probe with 50% and 90% of the measurement coming from within 1 and 3 mm, respectively, from the tip of the probe. To mitigate the effect of water content, two steps were taken: (1) the trench walls were left to dry for about a month after trench excavation, and (2) consecutive measurements were taken as quickly as practical to mitigate variation over time. Any residual effect of water content on the MS measurements is likely to reflect the variable capacity of different units to hold water. We accounted for temperature variations by calibrating the equipment after each profile and working through the night to avoid rapid temperature changes of the air, the trench sediments, and equipment caused by exposure to the sun. A small pilot study indicated that measurements of clasts larger than pebbles disrupted the overall MS pattern, which is displayed more clearly in the matrix. When survey points fell on a clast, we took the measurement as close as possible but not on the clast(s). Finally, we note that the measurement grid was offset horizontally by 10 cm from the string grid to minimize the effect of the metal nails used to fix the string grid to the sediment face.

The MS data were plotted using krigging with a variogram and a search radius that corrects for the sampling isotropy (Fig. 7). A low-pass Gaussian filter (5 columns 1.0 m wide and 5 rows 0.25 m high) was applied to smooth the data. The color scheme was iteratively selected to show the maximum contrast on the downthrown northern side of the fault.

Appendix B

Radiocarbon Dating Method

Charcoal fragments were handpicked from the sediment and subjected to the standard acid-base-acid (ABA) treatment. Samples were placed in clean 50 ml centrifuge tubes and immersed in 25 ml of 6N HCl at 70°C for 1 hr to remove carbonate sediments. The acid solution was decanted and replaced with 40 ml of 1N NaOH, which was held at 70°C for 30 min. This step is designed to remove humic acids (or humates) and other base-soluble organic compounds, which are typically considered to be contaminants (humic acids are soluble in groundwater and can move through the sediment column). Most samples did not contain significant quantities of humates, but it was necessary to repeat this step for a few samples until the base solution remained clear. Following the base step, samples were treated with 25 ml of 6N HCl at 70°C overnight to remove atmospheric carbon that was introduced during the previous step. Samples were then washed at least three times with 18.2 MΩ Milli-Q water and dried overnight in a vacuum oven at 70°C.

Approximately 4–6 mg of charcoal were placed in a Vycor tube with a 6 mm outside diameter along with cupric oxide (CuO) and silver foil that were precombusted at 900°C for 4 hr to eliminate contaminant carbon species. The tubes were evacuated overnight, cut off the extraction line with a glassblower's torch, and combusted at 850°C for 1 hr to convert organic carbon to CO_2. CO_2 was extracted and purified at Jay Quade's laboratory at the University of Arizona using standard cryogenic techniques and split into two aliquots. One aliquot (typically ~1 mg) was converted to graphite by catalytic reduction of CO (Slota *et al.*, 1987) and submitted to the AMS facility at the University of Arizona for ^{14}C analysis. The second aliquot (200–500 μg) was used to measure stable carbon isotope ratios in order to correct the measured ^{14}C content for fractionation. Stable isotope measurements are reported in the usual delta (δ) notation as the per mil (‰) deviation from the Peedee Belemnite (PDB) standard. Analytical uncertainties for $\delta^{13}C$ measurements are less than 0.1‰ based on repeated measurements of carbonate standards. All ^{14}C ages were converted to calendar ages using the IntCal04 calibration curve (Reimer *et al.*, 2004) in the OxCal program (see Data and Resources section). We report both the measured and calibrated ^{14}C ages and the corresponding $\delta^{13}C$ values for all experimental samples in Table A1.

To better understand how to interpret the reliability of our ^{14}C chronology, we needed to quantify the potential magnitude of contamination for samples that contained a significant amount of humates. For these samples, the basic solution decanted following the base step was reacidified with 10 ml of 6N HCl and allowed to stand overnight at room temperature. We isolated the humates precipitated during this step by centrifuging, decanting the supernatant, and drying them overnight at 70°C. We did not find a significant difference between ^{14}C ages obtained from the base-insoluble (or A) fraction and the base-soluble (or B) fraction for any of the paired samples (Table A1). We, therefore, consider our ^{14}C chronology based on charcoal to be extremely robust because of the apparent absence of different aged components. In other words, if contamination does exist in any given sample, the ^{14}C activity of the contaminant carbon is indistinguishable from the ^{14}C activity of the original sample material carbon. Although we generally consider ^{14}C ages derived from both the A and B fractions of the charcoal samples at Destek to be reliable, we still favor ages derived from A fractions when available because of the potential for contamination of B fractions via contaminants introduced by groundwater.

We evaluated the potential of using shell carbonate from the terrestrial gastropod Monarcha species because of the abundance of shell material in the sediments and its potential utility for dating earthquake events at Destek and other nearby sites. Terrestrial gastropods are often avoided for radiocarbon dating because they are known to incorporate carbon derived from limestone when building their shells (Goodfriend and Stipp, 1983). However, Pigati *et al.* (2004) found that some small terrestrial gastropod taxa did not incorporate dead carbon from limestone in their shells even when it was readily available. Those small taxa may yield reliable ^{14}C ages, therefore, regardless of the local lithology

Table A1

Summary of Experimental ^{14}C Results*

Evaluation of Live-Collected Gastropod Shell Carbonate

Sample Number	Trench Wall	Soil Unit	Lab Number	AMS Number	Taxa	$\delta^{13}C$	^{14}C Activity (FMC)	Atmospheric ^{14}C (FMC)	Difference† (FMC)
Das-X	N/A	Surface	DL-336	73280	Monarcha	−11.1	0.963 ± 0.004	1.06 ± 0.01	0.10 ± 0.01

Base-Soluble (A) and Base-Insoluble (B) Fractions of Charcoal

Sample Number	Trench Wall	Soil Unit	Lab Number	AMS Number	Taxa	$\delta^{13}C$	^{14}C Activity Unrounded	^{14}C Age (yr B.P.)* Unrounded	^{14}C Age (yr B.P.)* Rounded§	Calibrated Age‡ (yr B.P.)	Difference† (yr)
Das-181a	E	Col1	DL-407	75205	Charcoal (A)	−24.5	0.9740 ± 0.0036	212 ± 30	210 ± 30	178 ± 97	200 ± 110
Das-181b	E	Col1	DL-408	75206	Charcoal (B)	−24.8	0.9654 ± 0.0036	283 ± 30	280 ± 30	378 ± 61	
Das-18a	W	Col4a	DL-453	76611	Charcoal (A)	−24.7	0.8335 ± 0.0036	1407 ± 33	1410 ± 30	1316 ± 22	30 ± 40
Das-18b	W	Col4a	DL-454	76612	Charcoal (B)	−25.‖	0.8393 ± 0.0035	1463 ± 35	1460 ± 30	1350 ± 32	

Paired Gastropods and Charcoal Samples

Sample Number	Trench Wall	Soil Unit	Lab Number	AMS Number	Taxa and Fraction	$\delta^{13}C$	^{14}C Activity Unrounded	^{14}C Age (yr B.P.)* Unrounded	^{14}C Age (yr B.P.)* Rounded§	Calibrated Age‡ (yr B.P.)	Difference† (yr)
Das-200	E	Col1	DL-395	75201	Monarcha	−8.4	0.8496 ± 0.0033	1309 ± 31	1310 ± 30	1249 ± 37	970 ± 90
Das-181a	E	Col1	DL-407	75205	Charcoal (A)	−24.5	0.9740 ± 0.0036	212 ± 30	210 ± 30	178 ± 97	
Das-181b	E	Col1	DL-408	75206	Charcoal (B)	−24.8	0.9654 ± 0.0036	283 ± 30	280 ± 30	378 ± 61	
Das-281	E	Ps2a	DL-396	75202	Monarcha	−9.0	0.8587 ± 0.0033	1224 ± 31	1220 ± 30	1152 ± 55	650 ± 60
Das-114	W	Ps2a	DL-405	75204	Charcoal (A)	−24.9	0.9460 ± 0.0035	446 ± 30	450 ± 30	506 ± 26	
Das-192g	E	Ps3	DL-450	76608	Monarcha	−7.5	0.8859 ± 0.0034	973 ± 31	970 ± 30	862 ± 45	0 ± 60
Das-192c	E	Ps3	DL-460	76618	Charcoal (A)	−24.5	0.8859 ± 0.0034	973 ± 31	970 ± 30	862 ± 45	
Das-157	W	Col6e	DL-394	75200	Monarcha	−7.9	0.6408 ± 0.0026	3576 ± 33	3580 ± 30	3878 ± 53	700 ± 90
Das-51	W	Col6e	DL-404	76622	Charcoal (B)	−25.‖	0.6894 ± 0.0039	2987 ± 45	2990 ± 50	3176 ± 78	
Das-312	E	Ps5	DL-397	75203	Monarcha	−8.2#	0.6360 ± 0.0032	3635 ± 40	3630 ± 40	3950 ± 63	1120 ± 70
Das-309	E	Ps5	DL-409	75207	Charcoal (A)	−23.9	0.7103 ± 0.0028	2748 ± 32	2750 ± 30	2834 ± 40	

*Uncertainties for raw and calibrated 14C ages are given at the 1 σ (68%) confidence level.

†Absolute difference in sample ages. Uncertainties were summed quadratically. Ages and uncertainties were averaged for the two fractions of sample Das-181.

‡Unmodeled calibrated ages are determined using OxCal (see Data and Resources section). Unmodeled calibrated ages are median (i.e., equal probability before and after) $\pm 1\sigma$ standard deviation.

§Rounding follows convention (Stuiver and Polach, 1977).

‖$\delta^{13}C$ value not measured.

#$\delta^{13}C$ value estimated based on measurement of other Destek fossil gastropods ($n = 5$).

or environmental conditions. To determine if Monarcha species might also provide reliable ^{14}C ages, we measured the ^{14}C activity of a live-collected specimen living near the trench and compared it to the ^{14}C activity of the atmosphere during the time of collection. The ^{14}C activity (or fraction modern carbon [FMC]) of the shell carbonate (0.9633) was significantly lower than the atmospheric ^{14}C activity (Hua and Barbetti, 2004), which suggests that this species acquires ~10% of its shell carbon from limestone or other carbonate rocks. In the fossil record, such an offset would result in ^{14}C ages that were ~820 yr too old.

We also measured the ^{14}C content of five paired charcoal-gastropod samples to determine if this offset was constant through time. Fossil gastropod shells were cleaned from adhering sediment and detritus by sonication and multiple rinsing, followed by immersion in 3% H_2O_2 overnight at room temperature to further remove organic material. In all cases, the terrestrial gastropod shell carbon yielded ^{14}C ages that were older than the charcoal ^{14}C ages by an amount similar to that found in the live specimen (Table A1). Thus, when we had to use gastropod shell ages to constrain an event horizon, we assigned a correction factor of 0.085 ± 0.036 to the measured ^{14}C activity prior to calculating ^{14}C ages to account for this offset. This value represents the average difference between the measured ^{14}C activities of the shell and charcoal samples ($n = 5$); the uncertainty covers the full range of differences in the ^{14}C activities between paired samples.

To calibrate the age of specimens and constrain the timing of paleoearthquakes we have employed Bayesian statistical modeling techniques (Hilley and Young [2008] and references therein) using the OxCal program (see Data and Resources section). This method allows us to take into consideration the stratigraphic order of the samples and their associated probability distribution functions, and more importantly it allows us to determine the timing of paleoearthquakes to a known degree of certainty. On Figures 6, 7, and 9 the dates presented are the maximum and minimum of the 2 standard deviation OxCal modeled age range for the age of the samples. We also use the OxCal model to constrain the 2 standard deviation age of paleoearthquakes. Because we use this modeled approach, all of the sample ages we consider to be reliable affect the probability distribution functions of the other sample ages. Therefore, although we describe the timing of events being constrained by sample ages above and below event horizons, the age of the events are also affected by the other sample ages in the model (Ⓔ available in the electronic edition of *BSSA*).

Appendix C

Key for Trench Stratigraphy

This appendix provides descriptions for units defined in the Paleoseismic trench at Destek (Figs. 5–7 and 9) and discussed in the text.

Tac: topsoil, yellow-brown, silty gravel and sandy clay with some gravel, composed of organic and detrital material.

Col1: colluvium 1, yellow-brown, silty gravel with some clay, gravelly silt and silty gravel, matrix supported, composed of detrital material.

Col2: colluvium 2a, yellow-brown, gravelly silt and silty gravel with some clay and a trace of sand, matrix supported, composed of detrital material.

Col3a: colluvium 3a, yellow, sandy silty gravel with some clay and a trace of charcoal, matrix supported, composed of a range of clast lithologies.

Col3b: colluvium 3b, yellow-brown, gravelly silt with a trace of charcoal, matrix supported, composed of detrital material.

Col3c: colluvium 3c, yellow-brown, clayey gravelly silt with some sand and a trace of charcoal, composed of detrital material.

Col3d: colluvium 3d, yellow-brown, silty gravel with some clay and a trace of charcoal, composed of detrital material.

Col4a: colluvium 4a, yellow, gravelly silt with traces of clay and charcoal.

Col4b: colluvium 4b, yellow-brown, gravelly silt with a trace of charcoal.

Col4c: colluvium 4c, light yellow, silty clayey gravel, matrix supported, composed of detrital material with a recognizably high content of clast of the same material as Yex (extremely weathered yellow silt/claystone).

Col4d: colluvium 4d, yellow, silty clayey gravel with some sand, matrix supported, clasts composed of a range of lithologies (grades into Col5b at base locally).

Col5a: colluvium 5a, yellow, gravelly sandy silt with a trace of clay, matrix supported, clasts composed of a range of lithologies.

Col5b: colluvium 5b, yellow-brown, gravelly silty clay with some sand and a trace of charcoal, clasts composed of a range of lithologies (grades into underlying Cr2 locally, Col7a adjacently and overlying Col4d locally).

Col6a: colluvium 6a, brown, gravelly silt, clasts composed of a range of lithologies.

Col6b: colluvium 6b, brown, clayey silty gravel with a trace of sand, clasts composed of a range of lithologies.

Col6c: colluvium 6c, yellow-brown, gravelly silt with some clay, clasts composed with a range of lithologies.

Col6d: colluvium 6d, yellow-brown, sandy silty gravel, matrix supported, clasts composed of a range of lithologies.

Col6e: colluvium 6e, yellow, gravelly clay with a trace of sand, clast composed of a range of lithologies.

Col7a: colluvium 7a, yellow-brown, gravelly silty clay with some sand and a trace of charcoal, clasts composed of a range of lithologies (grades into overlying Col4d and *Col7a* adjacently locally).

Col7b: colluvium 7b, yellow, gravelly silty clay with some sand, clasts composed of a range of lithologies.

Col7c: colluvium 7c, yellow, clayey gravel, clast supported, clasts composed of a range of lithologies.

Col7d: colluvium 7d, yellow, gravelly silty clay with some sand, clasts composed of a range of lithologies.

Col7e: colluvium 7e, yellow, gravelly clayey silt with a trace of sand, clasts composed of a range of lithologies.

Col8a: colluvium 8a, brown, sandy silty clay with some gravel and a trace of charcoal.

Col8b: colluvium 8b, gray-brown, silty gravelly sand with some clay.

Col8c: colluvium 8c, brown, silty gravelly clay with some sand with a trace of charcoal.

Col8d: colluvium 8d, brown, silty clay with a trace of sand and charcoal.

Col8e: colluvium 8e, light yellow-brown, clayey silt with fine gravels encountered between −0.37 m and −0.42 m.

Col8f: colluvium 8f, light yellow-brown, gravelly clayey silt with some charcoal.

Col9a: colluvium 9a, brown, gravelly (medium) silty clay with a trace of sand and charcoal.

Col9b: colluvium 9b, yellow-brown, silty clayey gravel with some sand and a trace of charcoal.

Col9c: colluvium 9c, brown, sandy silty clay with some gravel and a trace of charcoal.

Col9d: colluvium 9d, brown, silty clay with a trace of sand and charcoal
Cola: colluvium A, yellow, silty gravel with some clay.
Colb: colluvium B, yellow-brown, gravelly silt and silty gravel with some clay and a trace of sand, matrix supported, composed of detrital material.
Colc: colluvium C, yellow, silty gravel.
Cold: colluvium D, orange-brown, gravelly clayey silt.
Cole: colluvium E, light yellow, silty clayey gravel, matrix supported, composed of detrital material with a recognizably high content of clast of the same material as Yex (extremely weathered yellow silt/claystone).
Colf: colluvium F, light yellow, silty clayey gravel, matrix supported, composed of detrital material with a recognizably high content of clast of the same material as Yex (extremely weathered yellow silt/claystone).
Ps1: paleosol 1, brown, gravelly silt, composed of detrital material with a trace of organic material.
Ps2a: paleosol 2a, brown, silty gravel, matrix supported, composed of detrital material with a trace of organic material.
Ps2b: paleosol 2b, brown, silt with some gravel, composed of detrital material with a trace of organic material.
Ps2c: paleosol 2c, brown, gravelly (fine) silt, composed of detrital material with a trace of organic material and brick fragments.
Ps3: paleosol 3, yellow-brown, clayey sandy silty gravel with a trace of charcoal, matrix supported, composed of mostly detrital material with some organic material.
Ps4: paleosol 4, yellow-brown, clayey gravelly silt with some charcoal and a trace of sand.
Ps5: paleosol 5, yellow-brown, gravelly clayey silt with a trace of sand, clasts composed of a range of lithologies.
Ps6: paleosol 6, brown and black, silty clayey charcoal with a trace of sand.
Ps7: paleosol 7, brown silty clayey gravel, with some charcoal, probably part of Ps2b.
IflA: fissure fill A, yellow-brown, gravelly (predominantly fine and angular) organic silt, massive.
IflB: fissure fill B, brown, gravelly silt, matrix supported at the base grading upward into clast supported silty gravel.
IflC: fissure fill C, brown-yellow, gravelly clayey silt with some sand.
CC1: concentrated charcoal layer 1, yellow-brown and black, clayey sandy silty gravel with a trace of charcoal, matrix supported, composed of mostly detrital material with up to 50% organic material locally.
Cr1: charcoal-rich layer 1, yellow-brown clayey gravelly silt with some sand and rich in charcoal.
Cr2: charcoal-rich layer 2, yellow-brown, silty clayey gravel rich in charcoal (grading into overlying Col5b locally), matrix supported, clasts composed of a range of lithologies.
Res1: residual soil 1, yellow, clayey silt with some sand and a trace of gravel, local remnants of parent rock laminations and fabric.
Res2: residual soil 2, red, clayey silt with some sand and a trace of gravel, local remnants of parent rock laminations and fabric.
KR: crushed rock, purple red, green, red and white, silty and sandy well graded angular gravel, various locally consistent lithologies.
Yex: yellow, extremely weathered laminated siltstone and claystone.
Rex: red, extremely weathered laminated siltstone and claystone.
Rock: red, yellow, green and white, highly sheared, coarse breccia with multiple lithologies (sedimentary and metamorphic).

Seismology Section
Royal Observatory of Belgium
Avenue Circulaire 3
1180 Brussels, Belgium
jeph4e@gmail.com
(J.F., A.H., K.V., U.A.)

U.S. Geological Survey
Box 25046, MS-980
Denver Federal Center
Denver, Colorado 80227
(J.S.P.)

Engineering Faculty, Department of Geology
Osmangazi University
Eskisehir, Turkey
(S.A.)

Manuscript received 9 April 2008